



ELSEVIER

Available online at www.sciencedirect.com

ScienceDirect

Comput. Methods Appl. Mech. Engrg. xxx (xxxx) xxx

**Computer methods
in applied
mechanics and
engineering**www.elsevier.com/locate/cma

Wavelet-enriched adaptive hierarchical FE model for coupled crystal plasticity-phase field modeling of crack propagation in polycrystalline microstructures

Jiahao Cheng^a, Xiaohui Tu^b, Somnath Ghosh^{c,*}^a Energy & Transportation Science Division, Oak Ridge National Laboratory, 1 Bethel Valley Road, Oak Ridge, TN 37831, United States of America^b Department of Civil Engineering, Johns Hopkins University, United States of America^c Departments of Civil, Mechanical and Material science Engineering, Johns Hopkins University, 3400 N. Charles St., Baltimore, MD 21218, United States of America

Received 8 July 2019; received in revised form 5 October 2019; accepted 14 November 2019

Available online xxx

Abstract

This paper develops a novel, wavelet-enriched adaptive finite element model for solving coupled crystal plasticity-phase field models to simulate crack propagation in polycrystalline microstructures. No *a-priori* assumption of the crack path is needed. Crack propagation under conditions of finite deformation is driven by stored elastic energy that accounts for material anisotropy and tension–compression asymmetry, and defect energy resulting from slip system dislocation glide and hardening. The resulting finite element model is capable of simulating both brittle and ductile crack propagation in material microstructures. A major contribution of this work is the creation of the adaptive, multi-resolution wavelet-based hierarchical enrichment of the FE model. The adapted enrichment follows the path of crack growth and is able to successfully overcome the challenges of high resolution required for the regularized crack in the coupled model. The multi-resolution wavelet basis functions adaptively construct optimal enrichment basis for the high gradients in the phase field order parameter near the crack path. The wavelet-enriched adaptive finite element model is found to be robust with excellent convergence characteristics in multiple validation tests conducted with the polycrystalline Ti–6V–4Al alloy.

© 2019 Elsevier B.V. All rights reserved.

Keywords: Crack propagation; Phase field; Crystal plasticity FE; Hierarchical finite element model; Adaptivity; Lifted second generation wavelets

1. Introduction

Modeling crack growth in polycrystalline materials, for which deformation is governed by crystal plasticity constitutive relations [1–5], is a difficult undertaking. Its implementation requires special consideration of the complex interaction between the propagating crack and deformation in the polycrystalline microstructure, characterized by crystallographic lattices, grain boundaries, twins, precipitates etc. Microstructural features like crystal lattice orientation, grain-boundary misorientation, micro-texture and twin boundaries can significantly affect the crack

* Corresponding author.

E-mail address: sghosh20@jhu.edu (S. Ghosh).<https://doi.org/10.1016/j.cma.2019.112757>

0045-7825/© 2019 Elsevier B.V. All rights reserved.

1 path and growth-rates. Depending on the microstructure, cracks surfaces are non-planar and can undergo kinking,
2 twisting or branching. In some materials, cracks propagate along the crystallographic cleavage planes. While crystal
3 plasticity-based computational models of deformation in polycrystalline materials are now mature [1–5], failure
4 prediction by intra-, trans- or inter-granular crack propagation in polycrystalline microstructures is still in its infancy.

5 A variety of alternative approaches have been proposed for modeling crack propagation in continuum media.
6 Many of these approaches use linear elastic fracture mechanics (LEFM) to model material cracking at the
7 macroscopic scale. The extended FEM or XFEM [6,7], generalized finite element methods [8,9], symmetric-Galerkin
8 boundary element method alternating with FEM or SGBEM-FEM [10], the discontinuous Galerkin approach [11,12]
9 and the cohesive zone models or CZM [13–16] introduce idealized surfaces in the computational domain for discrete
10 crack representation. In these methods, the crack propagation-rate and direction are determined by criteria that are
11 based on stress intensity factors or global energy release-rate. X-FEM can avert adaptive remeshing with crack
12 propagation since the mesh is generally independent of the crack geometry. However augmentation functions for
13 3D crack tip fields can be difficult to procure in the presence of plastic slip on crystalline lattices. Also the 3D
14 level-set functions that are conventionally used to represent crack surface topology can be very difficult with
15 inherent grain-scale heterogeneities of polycrystalline microstructures. CZMs, on the other hand, require cohesive
16 elements embedded between adjacent finite elements along the projected crack path with special traction–separation
17 constitutive relations. CZMs have been used in conjunction with crystal plasticity and discrete dislocation models
18 in [17,18] to simulate crack tip behavior and crack opening. A major shortcoming with CZMs in the polycrystalline
19 plasticity framework is that they require a-priori knowledge of 3D crack paths for inserting the traction–separation
20 laws in the computational model. These methods often require modification to the FE formulation, mesh adaptation,
21 element deletion or explicit mesh separation, which are computationally inefficient when dealing with cracks with
22 non-planar 3D surfaces. Nonlocal methods like peridynamics [19,20] have been successfully proposed to model
23 crack propagation predominantly in elastic media. While peridynamics formulations have been used for solving
24 crystal plasticity problems in [21], these methods are yet to model crack propagation in the context of crystal
25 plasticity.

26 Phase field (PF) models [22–27] have shown promise in overcoming some of the aforementioned difficulties,
27 and have received considerable attention from the fracture modeling community. This approach is based on the
28 regularization of a sharp crack surface through an auxiliary scalar field variable or order parameter $s \in [0, 1]$ to
29 represent the crack topology. The sharp crack discontinuity is approximated by a smooth transition between the
30 uncracked ($s = 0$) and fully-cracked ($s = 1$) material phases [28,29]. This is shown in the schematic Fig. 1(a).
31 The evolution of s with deformation and loading naturally models the crack growth process. An appealing feature
32 of the continuum phase field model is that it can be easily incorporated in a standard FEM framework, as it
33 implicitly tracks the crack phase without the need for remeshing due to discontinuous fracture surfaces. Relatively
34 few material parameters are needed in its representation. Phase field models for 3D crack branching and their
35 relation to fractographic patterns have been developed in [29,30]. Dynamic crack propagation with the phase field
36 models have been investigated in [30–34]. A fourth-order phase-field model of brittle fracture has been developed
37 and solved by isogeometric analysis in [33]. In [24,35–37] preferred cleavage planes are incorporated in oriented
38 grains by explicitly integrating the effect of grain orientation into phase field models. Comparison of phase field
39 models and LEFM has been made in [38–40].

40 This paper aims at modeling crack growth in polycrystalline microstructures, for which rate and temperature-
41 dependent crystal plasticity constitutive relations govern the material deformation. Image-based crystal plasticity
42 finite element (CPFE) models of statistically equivalent RVEs or SERVEs are solved e.g. in [4,41–43] for defor-
43 mation related fields in the polycrystalline microstructures. The SERVEs have crystallographic and morphological
44 distributions that are statistically equivalent to those obtained from experimental electron back-scatter diffraction
45 (EBSD) images. Fatigue crack nucleation in these microstructures has been predicted in [44–46] from variables
46 in CPFE simulations. The problem becomes significantly more challenging when changes in microstructural
47 topology occur with intra- and trans-granular crack propagation. Advanced phase field models have been developed
48 in [40,47,48] to study trans- and inter-granular fracture in materials with internal interfaces. A crystal plasticity
49 model has been coupled with phase field model in [49] for 2D analysis of ductile fracture in a single-crystal
50 Nickel-base superalloy. In [50], a kinematically linear crystal plasticity model has been combined with a phase
51 field model for ductile fracture in a single crystal material. A coupled crystal elasticity and phase field modeling
52 framework has been developed in [51] for simulating fracture processes in anisotropic elastic materials under finite
53 deformation conditions with crack-phase tension–compression asymmetry.

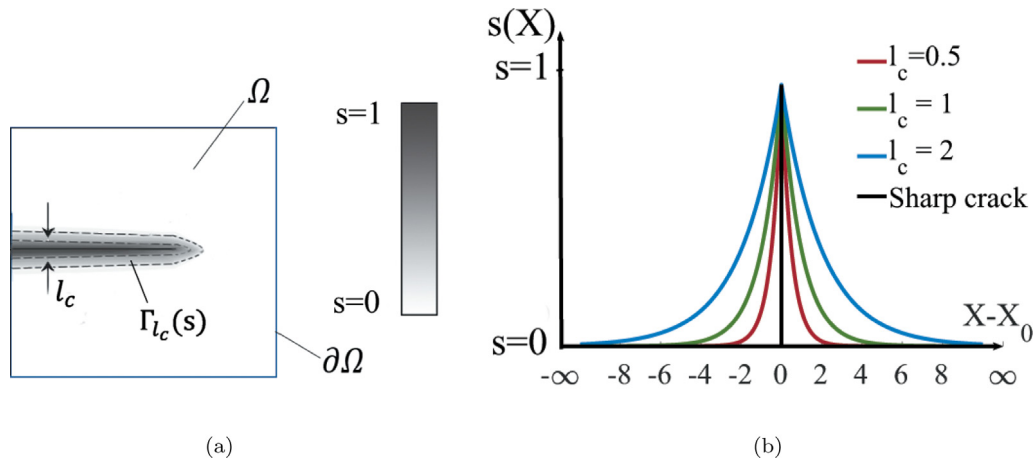


Fig. 1. (a) Illustration of a regularized sharp crack in the phase field representation with an order parameter $s \in [0, 1]$, and (b) regularized representation of a sharp crack at $X = 0$ with different length-scale parameters l_c .

A major bottleneck with phase field implementation of crack propagation in crystal plasticity FE models of polycrystalline microstructures is the requirement of very high mesh resolution, commensurate with the infinitesimally small length-scale of the order parameter s . A coarse finite element mesh cannot resolve the high gradient of s and may not effectively bound it to the theoretical range $[0, 1]$. For accurately tracking the crack, the element size must be sufficiently smaller than the characteristic physical length-scale of the crack. On the other hand, the typical converged mesh size for crystal plasticity analysis of grain-scale deformation variables is significantly larger. Without a-priori knowledge of the crack path, the coupled crystal plasticity-phase field FE model would require a highly refined mesh in its entirety to provide accurate mechanical driving forces near the crack tip. Such a high density mesh with large degrees of freedom for the coupled problem inevitably leads to prohibitively high computational costs especially for fatigue failure.

A few alternative approaches have been explored in the literature for accelerating phase field simulations. For example, GPU computing with compute unified device architecture (CUDA) has been used to accelerate phase field simulations in [52,53]. A non-intrusive global–local approach has been proposed in [54] for modeling brittle fracture in large-scale structure analysis. For polycrystalline microstructures, adaptive augmentation of mesh resolution with crack propagation is deemed to be a viable method for accelerating coupled crystal plasticity-phase field FE simulations and reducing computational costs. Adaptive methods generally rely on *a-posteriori* estimation of a solution error, followed by mesh refinement or *h-adaptation* [55,56], hierarchical enhancement of polynomial basis functions or *p-adaptation* [57,58] or their combination [59,60]. However, many of the above strategies do not guarantee conformity of the new enriched space to the profile of the crack phase field solution s . Moreover, old shape functions are not preserved in the new enriched solution space, which adds to the difficulty of mapping internal variables.

An adaptive wavelet-based hierarchical enrichment method has been proposed for crystal elasticity and crystal plasticity finite element modeling of polycrystalline microstructures in [61] and [62] respectively. Rather than evaluating error indicators, the method adaptively creates an optimal discretization space conforming to the solution profile by projecting the solution field onto a set of scaling and multi-resolution wavelet basis functions. A fine-scale solution profile is estimated from a computationally efficient coarse mesh solution using a modified Jacobi iterative solver. This solution profile is subsequently represented using a fast wavelet transform and compression method with identification of the optimal discretization basis. Second generation family of wavelets [63–65] is used to generate hierarchical functions that are compatible with finite element shape functions on an irregular mesh. This wavelet-based adaptive method is advantageous for constructing an optimal set of enrichment functions that conform to the solution space, rendering it appropriate for solving the coupled crystal plasticity-phase field problems.

This paper begins with a discussion of governing equations for the coupled crystal plasticity and phase field crack model in Section 2. The finite element formulation and numerical implementation of the coupled model are discussed in Section 3. Section 4 examines mesh-dependence issues and introduces wavelet-based adaptive

1 hierarchical finite element formulation and implementation algorithms. A discussion of the wavelet basis functions
 2 and some numerical implementation issues are commenced in Section 5. Simulations are conducted for the titanium
 3 alloy Ti-6V-4Al in Section 6. Convergence rates, solution errors and crack path characteristics are examined for two
 4 computational microstructures of the polycrystalline material. The paper concludes with a summary in Section 7.

5 2. Governing equations for the coupled crystal plasticity and phase field crack model

6 The phase field formulation of crack propagation is developed within the framework of crystal plasticity finite
 7 element model for polycrystalline microstructures in this paper. The crack phase field and its gradient regularize the
 8 geometric features of the sharp crack topology. Crack evolution results in energy dissipation by releasing both the
 9 elastic stored energy and the defect energy of plastic work. The coupled crystal plasticity and phase field constitutive
 10 relations, describing the dissipation process result from thermodynamic principles with the crack geometric function.

11 2.1. Crystal plasticity kinematic relations

12 Consider a continuum body occupying a domain $\Omega \in \mathcal{R}^3$ and undergoing finite deformation described by the
 13 deformation gradient tensor \mathbf{F} ($= \partial \mathbf{x} / \partial \mathbf{X}$), where \mathbf{x} ($= \mathbf{u} + \mathbf{X}$) and \mathbf{X} are respectively the Cartesian coordinates of a
 14 material point in the current and reference configuration and \mathbf{u} is the displacement vector. In the crystal plasticity
 15 formulation e.g. in [2,4,41,42,66] the deformation gradient is multiplicatively decomposed into elastic and plastic
 16 parts, expressed as

$$17 \quad \mathbf{F} = \mathbf{F}^e \mathbf{F}^p \quad (1)$$

18 Crystal plasticity kinematics assumes the existence of N_{slip} slip systems of dislocation glide. Each slip system
 19 is characterized by a slip plane with unit normal \mathbf{n}^α and a slip direction vector \mathbf{m}^α . The collective motion of
 20 dislocations gliding on each slip system α with a slip-rate $\dot{\gamma}^\alpha$ causes plastic flow. The corresponding plastic velocity
 21 gradient tensor is expressed in terms of the slip-rate on each slip system α as:

$$22 \quad \mathbf{L}^p = \dot{\mathbf{F}}^p \mathbf{F}^{p-1} = \sum_{\alpha=1}^{N_{slip}} \dot{\gamma}^\alpha \mathbf{m}_0^\alpha \otimes \mathbf{n}_0^\alpha \quad (2)$$

23 where \mathbf{n}_0^α and \mathbf{m}_0^α are respectively the slip plane unit normal and the slip direction vector in the reference
 24 configuration. A power law model is used for representing the plastic slip rate $\dot{\gamma}^\alpha$ on the α -th slip system in terms
 25 of the resolved shear stress τ^α and the slip system deformation resistance g^α , and is expressed as:

$$26 \quad \dot{\gamma}^\alpha = \dot{\gamma}_0 \left| \frac{\tau^\alpha}{g^\alpha} \right|^{1/m} \text{sign}(\tau^\alpha) \quad (3)$$

27 Here m is the material rate sensitivity parameter and $\dot{\gamma}_0$ is the reference plastic shearing rate. The evolution of slip
 28 system deformation resistance is assumed to be controlled by statistically stored dislocations due to homogeneous
 29 plastic deformation. The corresponding rate of deformation resistance for a slip system α is expressed as:

$$30 \quad \dot{g}^\alpha = \sum_{\beta}^{N_{slip}} h^{\alpha\beta} |\dot{\gamma}^\beta| \quad \text{where } h^{\alpha\beta} = q^{\alpha\beta} h^\beta \quad (\text{no sum on } \beta) \quad (4)$$

31 The anisotropic hardening modulus $h^{\alpha\beta}$ corresponds to the strain hardening rate due to self and latent hardening on
 32 the α -th slip system by slip on the β -th slip system respectively. Here, h^β is the self hardening coefficient and $q^{\alpha\beta}$
 33 is a matrix describing latent hardening. The evolution laws for h^β have been given in [67,68]. The above relations
 34 are derived in the context of defect energy due to dislocations in Section 2.3.2.

35 2.2. Phase field description of the crack

36 The phase field model introduces a continuous order parameter s field to describe the discrete crack topology. It
 37 represents the discrete crack interface Γ by a functional $\Gamma_c(s)$. In 1-D, the mathematical form of $\Gamma_c(s)$ is derived

from an exponential approximation of the s field. The regularization of a sharp crack discontinuity is represented by the s field as:

$$s(X) = e^{-\frac{|X-X_0|}{l_c}} \quad (5)$$

where X and X_0 are respectively the coordinates of a point in the regularized s domain and its origin, corresponding to the location of the sharp crack discontinuity and $|X - X_0|$ is the relative distance. l_c is a length-scale parameter that controls the sharpness of the regularization function [22]. As shown in Fig. 1(b), the s field recovers the sharp crack geometry in the limit $l_c \rightarrow 0$. From Eq. (5), $s(X_0) = 1$ corresponds to a fully cracked point and $\lim_{X \rightarrow \pm\infty} s(X) = 0$. The expression for s in Eq. (5) is the solution of the Euler–Lagrange equation for the variational problem stated as:

$$s = \text{Arg} \left\{ \inf_{s \in w} \Pi(s) \right\} \quad \text{for} \quad \Pi(s) = \frac{1}{2} \int_{\Omega} \left\{ s^2 + l_c^2 \left(\frac{ds}{dX} \right)^2 \right\} d\Omega \quad (6)$$

where $w = \{s | s(X_0) = 1, \text{ and } s(\pm\infty) = 0\}$ corresponds to the Dirichlet boundary condition. For the cross-sectional area of the cracked bar denoted by Γ , the incremental volume is $d\Omega = \Gamma dX$. Substituting s from Eq. (5) to $\Pi(s)$ in Eq. (6) establishes the relation $\Pi(S) = \Gamma l_c$. The regularized crack surface area functional in the phase field model can therefore be expressed as:

$$\Gamma_l(s) = \int_{\Omega} \gamma_l d\Omega \quad \text{where} \quad \gamma_l = \frac{1}{2l_c} \left\{ s^2 + l_c^2 \left(\frac{ds}{dX} \right)^2 \right\} \quad (7)$$

In the limit $l_c \rightarrow 0$, $\inf_{s \in w} \Gamma_l(s)$ restores the geometry of the sharp crack interface Γ . For 3D problems, Eq. (7) can be extended to the 3D regularized crack surface density function as:

$$\gamma_l = \frac{1}{2l_c} (s^2 + l_c^2 \nabla_{\mathbf{X}} s \cdot \nabla_{\mathbf{X}} s) \quad (8)$$

where $\nabla_{\mathbf{X}}$ corresponds to the spatial derivative vector with respect to the reference coordinates.

2.3. Helmholtz free energy density of degrading material undergoing finite elasto-plastic deformation

The crystal plasticity-based finite deformation fields and the crack phase field are coupled through a Helmholtz free energy density (HFED) function in the reference configuration. The stored energy density contributions are due to elastic stretching of the crystal lattice, as well as due to defect formation, e.g. dislocation density evolution with plastic deformation. With material degradation due to crack evolution the stored energy is released locally in the form of a crack surface energy. For simulating finite deformation in elastic–plastic crystalline materials with material degradation, the HFED function in the reference configuration $\rho_0 \psi$ is assumed to be the sum of contributions from each of the three mechanisms, expressed as:

$$\rho_0 \psi = \rho_0 \psi_e(\mathbf{E}^e, s) + \rho_0 \psi_d(\boldsymbol{\eta}, s) + \rho_0 \psi_c(s, \nabla_{\mathbf{X}} s) \quad (9)$$

where ρ_0 is the material density in the reference configuration. The elastic energy per unit mass ψ_e is a function of the elastic part of the Green–Lagrange strain defined as $\mathbf{E}^e = \frac{1}{2}(\mathbf{F}^{eT} \mathbf{F}^e - \mathbf{I})$ and the phase field order parameter s . The second term ψ_p is the stored defect energy density per unit mass due to the population of defect structures such as sessile dislocations and dislocation cell walls [69]. It is a function of a set of internal variables $\boldsymbol{\eta}$ representing microscopic defects, as well as s . The dependence of both the stored elastic energy ψ_e and the defect energy ψ_d of the material degradation state s is due to the fact that crack propagation requires the release of both these energy components. Finally, the crack surface energy per unit mass ψ_c is defined by a Griffith-type fracture energy per unit area g_c and the regularized crack surface density function γ_l given in Eq. (8), as:

$$\rho_0 \psi_c = \frac{g_c}{2l_c} (s^2 + l_c^2 \nabla_{\mathbf{X}} s \cdot \nabla_{\mathbf{X}} s) \quad (10)$$

The simulations in this work are conducted under isothermal conditions and hence the evolution of temperature fields is not accounted for a thermal energy in Eq. (9).

2.3.1. Finite deformation anisotropic elastic energy with tension–compression asymmetry for evolving cracks

Modeling crack propagation in polycrystalline materials requires incorporation of finite deformation kinematics in anisotropic crystalline materials. Furthermore, the crack surface behavior is governed by unilateral conditions of stress carrying capacity depending on the state of strain i.e. compressive vs. tensile [70]. In tension, the crack surfaces open up causing a loss of stress-carrying capacity, while under compression, the crack surfaces close allowing the stress to be transmitted across the crack surfaces. Various stored elastic energy density functions has been proposed for phase field fracture theory, e.g. in [22,24,28,71] for isotropic materials undergoing infinitesimal strains. However, they are generally not applicable for modeling polycrystalline microstructures, for which each individual grain is intrinsically anisotropic and undergo finite deformation.

For an undamaged anisotropic material that is characterized by anisotropic crystallographic lattices, the elastic part of the Helmholtz free energy density (HFED) in Eq. (9) may be expressed as [51]:

$$\rho_0 \psi_e(\mathbf{E}^e, s) = \frac{1}{2} \mathbf{E}^e(s) : \mathbb{C}^e : \mathbf{E}^e(s) \quad (11)$$

where \mathbb{C}^e denotes the fourth-order anisotropic elasticity tensor at a material point expressed in the material symmetry coordinate system, and $\mathbf{E}^e(s) = \frac{1}{2}(\mathbf{F}^{eT} \mathbf{F}^e - \mathbf{I})$ is the elastic part of the Green–Lagrange strain tensor. A phase field parameter s dependent degradable Green–Lagrange elastic strain tensor $\tilde{\mathbf{E}}^e$ has been proposed in [51] for a coupled FE-phase field model to simulate crack evolution in elastic polycrystalline microstructures. The degradable strain tensor $\tilde{\mathbf{E}}^e$ is formulated to represent tension–compression asymmetry of crack fields in the HFED expression under finite strain conditions. It is obtained from isochoric–volumetric decomposition of the elastic deformation gradient, i.e.:

$$\mathbf{F}^e = \mathbf{F}_{iso}^e \mathbf{F}_{vol}^e \quad (12)$$

where $\mathbf{F}_{iso}^e = (\det \mathbf{F}^e)^{-\frac{1}{3}} \mathbf{F}^e$ is the isochoric deformation gradient, and $\mathbf{F}_{vol}^e = (\det \mathbf{F}^e)^{\frac{1}{3}} \mathbf{I}$ is the volumetric deformation gradient. The degradable elastic Green–Lagrange strain tensor is then expressed as:

$$\tilde{\mathbf{E}}^e = g_1(J^e, s) \mathbf{E}_{vol}^e + g_2(s) \mathbf{E}^e \quad (13a)$$

$$\text{with } g_1(J^e, s) = \mathcal{H}(1 - J^e)(1 - \kappa_s)s \quad \text{and} \quad g_2(s) = 1 - (1 - \kappa_s)s \quad (13b)$$

The volumetric part of the Green–Lagrangian elastic strain tensor is $\mathbf{E}_{vol}^e = \frac{1}{2}(\mathbf{F}_{vol}^{eT} \mathbf{F}_{vol}^e - \mathbf{I})$ and $J^e = \det \mathbf{F}^e$ is the elastic Jacobian. $\mathcal{H}(x)$ represents the Heaviside step function. Since plastic deformation is assumed to be isochoric, $J^e > 1$ indicates a tensile volume change while $J^e < 1$ indicates a volume change in compression. If the volume change is tensile, both components of $\tilde{\mathbf{E}}^e$ in Eq. (13) are degraded with s . However, if the volume change is compressive, the volumetric strain in the first component is unaffected. κ_s is a small positive parameter that is incorporated to prevent complete vanishing of the local stiffness that can lead to numerical difficulties [28]. In this work, a small value $\kappa_s = 0.001$ is assumed.

The anisotropic elastic energy density in Eq. (11) is consequently modified for a material undergoing crack evolution in the form of the evolving phase field parameter s as:

$$\rho_0 \psi_e = \frac{1}{2} \tilde{\mathbf{E}}^e : \mathbb{C}^e : \tilde{\mathbf{E}}^e \quad (14)$$

In this HFED expression (14), the isochoric part of the elastic strain always degrades with the evolving phase field order parameter s , whereas the volumetric part is degraded only if the volume change is positive corresponding to a tensile state. Note that since the degradation is operated only on the strain tensor, the anisotropic elastic stiffness matrix \mathbb{C}^e is unchanged by the phase field.

2.3.2. Degradable defect energy for crystal plasticity induced deformation

In the crystal plasticity constitutive framework, dislocation densities increase with slip due to expansion of dislocation loops, interaction of gliding dislocations with forest dislocations and formation of dislocation junctions, jogs and dislocation cell walls. These structures act as barriers to gliding dislocations. Further elastic stretching is required to overcome the barriers resulting in hardening. While the additional elastic stretch of the crystal lattice continues to increase the stored elastic strain energy, it also adds to the local dislocation structures resulting in higher defect energies. The degrading, stored defect energy density is assumed to be of the form:

$$\rho_0 \psi_d(\boldsymbol{\eta}, s) = g(s) \rho_0 \hat{\psi}_d(\boldsymbol{\eta}) \quad (15)$$

where $\hat{\psi}_d(\boldsymbol{\eta})$ is a non-degraded defect energy per unit mass and $g(s) = (1 - s)$ is a degradation function. Consider that the defects are in the form of dislocations on N_{slip} systems. Following [69], a simple quadratic form may be used to define the defect energy density as:

$$\rho_0 \hat{\psi}_d(\boldsymbol{\eta}) = \frac{1}{2} \sum_{\alpha, \beta}^{N_{slip}} h^{\alpha\beta} |\eta^\alpha| |\eta^\beta| \quad (16)$$

where η^α and η^β are the internal variables corresponding to defects (dislocations) on the α and β slip systems respectively, and $h^{\alpha\beta}$ is the anisotropic hardening modulus matrix defined in Eq. (4) of Section 2.1. It describes the contribution from the interactions between slip systems α and β to the defect energy.

It is common to invoke the principle of maximum plastic dissipation for deriving the special form of η^α . The non-negative plastic dissipation-rate density \mathcal{D}^p is defined as the internal plastic power density minus the stored defect energy density, and expressed as:

$$\begin{aligned} \mathcal{D}^p &= \boldsymbol{\Xi} : \mathbf{L}^p - \rho_0 \dot{\hat{\psi}}_d(\boldsymbol{\eta}) = \mathbf{F}^{eT} \mathbf{F}^e \mathbf{S} : \sum_{\alpha}^{N_{slip}} \dot{\gamma}^\alpha (\mathbf{m}_0^\alpha \otimes \mathbf{n}_0^\alpha) - \sum_{\alpha}^{N_{slip}} \rho_0 \frac{\partial \hat{\psi}_d}{\partial \eta^\alpha} \dot{\eta}^\alpha \\ &= \sum_{\alpha}^{N_{slip}} \tau^\alpha \dot{\gamma}^\alpha - \sum_{\alpha}^{N_{slip}} g^\alpha \dot{\eta}^\alpha \geq 0 \end{aligned} \quad (17)$$

where \mathbf{S} is the second Piola–Kirchhoff stress. The term $\boldsymbol{\Xi} : \mathbf{L}^p$ is deduced from the equations

$$\int_{\Omega} \boldsymbol{\sigma} : \mathbf{L} \, d\Omega = \int_{\Omega_0} \boldsymbol{\tau} : (\mathbf{L}^e + \mathbf{L}^p) \, d\Omega_0 = \int_{\Omega_0} \boldsymbol{\tau} : \dot{\mathbf{F}}^e \mathbf{F}^{e-1} + \boldsymbol{\tau} : \mathbf{F}^e \mathbf{L}^p \mathbf{F}^{e-1} \, d\Omega_0$$

and

$$\int_{\Omega_0} \boldsymbol{\tau} : \mathbf{F}^e \mathbf{L}^p \mathbf{F}^{e-1} \, d\Omega_0 = \int_{\Omega_0} \boldsymbol{\Xi} : \mathbf{L}^p \, d\Omega_0$$

where $\boldsymbol{\sigma}$ and $\boldsymbol{\tau}$ are respectively the Cauchy stress and Kirchhoff stress tensor. $\boldsymbol{\Xi} (= \mathbf{F}^{eT} \boldsymbol{\tau} \mathbf{F}^{e-T} = \mathbf{F}^{eT} \mathbf{F}^e \mathbf{S})$ is the Mandel stress, which is the power conjugate to \mathbf{L}^p and is convenient to use for finite strain plasticity. \mathbf{L} and \mathbf{L}^e are the total and elastic velocity gradient tensors respectively. $\tau^\alpha = \mathbf{F}^{eT} \mathbf{F}^e \mathbf{S} : (\mathbf{m}_0^\alpha \otimes \mathbf{n}_0^\alpha)$ is the resolved shear stress on the α -th slip system and $g^\alpha \equiv \frac{\partial \hat{\psi}_d}{\partial \eta^\alpha} \eta^\alpha$ is the thermodynamic hardening stress [72].

The constitutive relation for the defect internal variable η^α is first examined for rate-independent crystal plasticity theory. The results are consequently generalized to rate-dependent crystal plasticity constitutive framework. The rate-independent crystal plasticity theory is based on a yield surface on each slip system α , written as:

$$f^\alpha = |\tau^\alpha| - (g_0^\alpha + g^\alpha) \quad (18)$$

where g_0^α is a constant initial slip resistance. Taking the yield surface as a constraint, the constrained dissipation function may be expressed using Lagrangian multiplier as:

$$\mathcal{L}(\tau^\alpha, g^\alpha) = \mathcal{D}^p - \lambda^\alpha f^\alpha = \left\{ \sum_{\alpha}^{N_{slip}} (\tau^\alpha \dot{\gamma}^\alpha - g^\alpha \dot{\eta}^\alpha) \right\} - \lambda^\alpha \{ |\tau^\alpha| - (g_0^\alpha + g^\alpha) \} \quad (19)$$

where λ^α is the Lagrange multiplier on α slip system, that is subject to the Kuhn–Tucker complementarity conditions:

$$\lambda^\alpha \geq 0, \quad f^\alpha \leq 0, \quad \lambda^\alpha f^\alpha = 0 \quad (20)$$

The extremum of $\mathcal{L}(\tau^\alpha, g^\alpha)$ yields the plasticity relations for the internal variables, expressed as:

$$\nabla \mathcal{L} = 0 \Rightarrow \begin{cases} \frac{\partial \mathcal{L}}{\partial \tau^\alpha} = 0 \Rightarrow \dot{\gamma}^\alpha = \lambda^\alpha \text{sign}(\tau^\alpha) \\ \frac{\partial \mathcal{L}}{\partial g^\alpha} = 0 \Rightarrow \dot{\eta}^\alpha = \lambda^\alpha = |\dot{\gamma}^\alpha| \end{cases} \quad (21)$$

Thus, reasonable choices for the defect internal variable η^α and the non-degraded stored defect energy density $\hat{\psi}_d$ are :

$$\eta^\alpha = |\gamma^\alpha|, \quad \text{and} \quad \rho_0 \hat{\psi}_d(\boldsymbol{\eta}) = \frac{1}{2} \sum_{\alpha, \beta}^{N_{slip}} h^{\alpha\beta} |\gamma^\alpha| |\gamma^\beta| \quad (22)$$

Combining equations (16) and (22) along with the definition of the thermodynamic hardening stress $g^\alpha \equiv \frac{\partial \hat{\psi}_d}{\partial \eta^\alpha} \eta^\alpha$, and assuming symmetry of $h^{\alpha\beta}$, the crystal plasticity hardening relation is obtained as:

$$\dot{g}^\alpha = \sum_{\beta}^{N_{slip}} h^{\alpha\beta} |\dot{\gamma}^\beta| \quad (23)$$

For rate-dependent power-law type crystal plasticity model, a Norton–Hoff type viscoplastic regularization of the above procedure is employed. The yield function for each slip system is expressed as:

$$\hat{f}^\alpha = \frac{\dot{\gamma}_0 (g_0^\alpha + g^\alpha)}{\frac{1+m}{m}} \left[|\Phi|^{\frac{1+m}{m}} - 1 \right] \quad \text{where} \quad \Phi = \frac{\tau^\alpha}{g_0^\alpha + g^\alpha} \quad (24)$$

Here $\dot{\gamma}_0 (> 0)$ is the reference slip-rate and $m > 0$ is the strain-rate sensitivity parameter as given in Section 2.1. In contrast to the static yield surface equation (18),

$$\hat{f}^\alpha > 0 \quad \text{for} \quad \tau - (g_0^\alpha + g^\alpha) > 0 \quad \text{and} \quad \hat{f}^\alpha \leq 0 \quad \text{for} \quad |\tau| - (g_0^\alpha + g^\alpha) \leq 0 \quad (25)$$

The state $\Phi > 1$ is an overshoot of the stress state beyond the static yield surface. The Kuhn–Tucker complementarity conditions are not needed for this case, as all slip systems are active at all times. The constraint \hat{f}^α is applied as a penalty function in the plastic dissipation function as:

$$\mathcal{L}(\tau^\alpha, g^\alpha) = \mathcal{D}^p - \hat{f}^\alpha \quad (26)$$

Analogous to Eq. (21), the extremum conditions of Eq. (26) is sought from the relations $\frac{\partial \mathcal{L}}{\partial \tau^\alpha} = 0$ and $\frac{\partial \mathcal{L}}{\partial g^\alpha} = 0$. These respectively leads to the power-law equation for the slip-rates, as well as the relation for the defect variables as:

$$\dot{\gamma}^\alpha = \dot{\gamma}_0^\alpha \left| \frac{\tau^\alpha}{g_0^\alpha + g^\alpha} \right|^{\frac{1}{m}} \text{sign}(\tau^\alpha) \quad (27a)$$

$$\dot{\eta}^\alpha \cong |\dot{\gamma}^\alpha| \quad (27b)$$

The defect equation (27b) makes the plastic dissipation \mathcal{D}^p non-negative. It suggests the selection of the same defect variable and defect energy form as in Eq. (22), as well as the hardening of Eq. (23). The anisotropic hardening modulus matrix $h^{\alpha\beta}$ (also discussed in Eq. (4)) has been constructed in various forms for different crystal plasticity models. In the present work, a form suggested in [67,68] is used:

$$h^{\alpha\beta} = q^{\alpha\beta} h^\beta, \quad h^\beta = h_0^\beta \left| 1 - \frac{g^\beta}{g_s^\beta} \right|^r \text{sign} \left(1 - \frac{g^\beta}{g_s^\beta} \right), \quad g_s^\beta = \tilde{g} \left(\frac{\dot{\gamma}^\beta}{\dot{\gamma}} \right)^n \quad (28)$$

Here $q^{\alpha\beta}$, h_0^β , r , \tilde{g} and $\dot{\gamma}$ are constant hardening parameters. This establishes the stored defect energy density in the HEFD, consistent with classical crystal plasticity power-law slip-rate model of Eq. (27a) and hardening relations in Eqs. (23) and (28).

2.4. Equilibrium equations and constitutive relations for the coupled mechanical and crack phase field problem

The equilibrium equation and constitutive relations for the coupled deformation and crack propagation problem are derived from the principle of virtual power and laws of thermodynamics.

2.4.1. Equilibrium equations

For the two-field (\mathbf{u}, s) problem in the domain Ω with boundary $\partial\Omega$, it is necessary to first specify the boundary and loading conditions for each solution field. The Dirichlet conditions on the displacement and crack phase fields

are respectively specified as:

$$\mathbf{u} = \bar{\mathbf{u}} \text{ on } \Gamma_{0u} \quad \text{and} \quad s = \bar{s} \text{ on } \Gamma_{0s}$$

where Γ_{0u} and Γ_{0s} are boundary segments in the reference configuration, where displacement $\bar{\mathbf{u}}$ and phase field \bar{s} boundary conditions are imposed respectively. The domain is subject to external mechanical traction loadings $\mathbf{T} = \bar{\mathbf{T}}$ on boundary Γ_{0T} in the reference configuration. Furthermore, the domain is also subjected to external microscopic traction $\lambda_0 = \bar{\lambda}_0$, which is power-conjugate to the rate of phase field variable \dot{s} and applied on boundary $\Gamma_{0\lambda}$ in the reference configuration. It is noteworthy that boundary segments for the displacement field and phase field can be overlapping, i.e.

$$\Gamma_{0T} \cap \Gamma_{0u} = \emptyset, \quad \Gamma_{0T} \cup \Gamma_{0u} = \partial\Omega_0 \quad (29a)$$

$$\Gamma_{0\lambda} \cap \Gamma_{0s} = \emptyset, \quad \Gamma_{0\lambda} \cup \Gamma_{0s} = \partial\Omega_0 \quad (29b)$$

Additionally, the body is also subject to an external body force \mathbf{B} that is power-conjugate to the velocity field $\dot{\mathbf{u}}$, and an external microscopic body force l_0 , which is power-conjugate to \dot{s} , both in the reference configuration. The virtual power δP_{ext} on Ω due to external loadings is written as:

$$\delta P_{ext} = \int_{\Gamma_{0T}} \mathbf{T} \cdot \delta \dot{\mathbf{u}} \, d\Gamma_{0T} + \int_{\Omega_0} \mathbf{B} \cdot \delta \dot{\mathbf{u}} \, d\Omega_0 + \int_{\Gamma_{0\lambda}} \lambda_0 \delta \dot{s} \, d\Gamma_{0\lambda} + \int_{\Omega_0} l_0 \delta \dot{s} \, d\Omega_0 \quad (30)$$

where $\delta \dot{\mathbf{u}} \in V^u$ and $\delta \dot{s} \in V^s$ are respectively the virtual velocity and virtual rate of s , defined as:

$$V^u = \left\{ \delta \dot{\mathbf{u}} \in H^1(\Omega), \quad \delta \mathbf{u} = \mathbf{0} \text{ on } \Gamma_{0u} \right\} \quad (31a)$$

$$V^s = \left\{ \delta \dot{s} \in H^1(\Omega), \quad \delta s = 0 \text{ on } \Gamma_{0s} \right\} \quad (31b)$$

Following [50], the virtual internal power for the body in equilibrium in the absence of inertia, is written as:

$$\delta P_{int} = \int_{\Omega_0} \mathbf{P} : \delta \dot{\mathbf{F}} \, d\Omega_0 + \int_{\Omega_0} \boldsymbol{\xi}_0 \cdot \nabla_{\mathbf{X}} \delta \dot{s} \, d\Omega_0 + \int_{\Omega_0} \pi_0 \delta \dot{s} \, d\Omega_0 \quad (32)$$

where the first term in the right hand side (RHS) corresponds to the internal virtual work done with the virtual displacement field, \mathbf{P} is the first Piola–Kirchhoff stress. \mathbf{P} is the power conjugate to $\dot{\mathbf{F}}$ that can be related to other stress measures as:

$$\int_{\Omega_0} \mathbf{P} : \dot{\mathbf{F}} \, d\Omega_0 = \int_{\Omega_0} \mathbf{S} : \dot{\mathbf{E}} \, d\Omega_0 = \int_{\Omega_0} \boldsymbol{\tau} : \mathbf{D} \, d\Omega_0 \quad (33)$$

The last two terms in the RHS of Eq. (32) correspond to the internal virtual work done on the virtual phase field. $\boldsymbol{\xi}_0$ is the microscopic stress-like vector, which is the power-conjugate to $\nabla_{\mathbf{X}} \dot{s}$, and π_0 is an microscopic force-like scalar that is power-conjugate to \dot{s} , both in the reference configuration.

Combining equations (30) and (32) yields the principle of virtual power for the mechanical problem as:

$$\int_{\Gamma_{0T}} \mathbf{T} \cdot \delta \dot{\mathbf{u}} \, d\Gamma_{0T} + \int_{\Omega_0} \mathbf{B} \cdot \delta \dot{\mathbf{u}} \, d\Omega_0 = \int_{\Omega_0} \mathbf{S} : \nabla_{\mathbf{X}} \delta \dot{\mathbf{u}} \, d\Omega_0 \quad (34)$$

which reduces to the governing equation of equilibrium and traction law for the displacement field in the reference configuration as:

$$\nabla_{\mathbf{X}} \cdot \mathbf{P} + \mathbf{B} = \mathbf{0} \quad \forall \mathbf{X} \in \Omega_0 \quad \text{and} \quad \mathbf{T} = \mathbf{P} \mathbf{N} \quad \forall \mathbf{X} \in \Gamma_{0T} \quad (35)$$

\mathbf{N} is unit normal vector to the boundary in the reference configuration. In a similar manner, the principle of virtual power for the phase field problem is obtained as:

$$\int_{\Gamma_{0\lambda}} \lambda_0 \delta \dot{s} \, d\Gamma_{0\lambda} + \int_{\Omega_0} l_0 \delta \dot{s} \, d\Omega_0 = \int_{\Omega_0} \boldsymbol{\xi}_0 \cdot \nabla_{\mathbf{X}} \delta \dot{s} \, d\Omega_0 + \int_{\Omega_0} \pi_0 \delta \dot{s} \, d\Omega_0 \quad (36)$$

This leads to the equilibrium equation and traction law for the crack phase field problem in the reference configuration as:

$$\nabla_{\mathbf{X}} \cdot \boldsymbol{\xi}_0 - \pi_0 + l_0 = 0 \quad \forall \mathbf{X} \in \Omega_0 \quad \text{and} \quad \lambda_0 = \boldsymbol{\xi}_0 \cdot \mathbf{N} \quad \forall \mathbf{X} \in \Gamma_{0\lambda} \quad (37)$$

2.4.2. Constitutive relations

The constitutive relations for the crack propagation driving force ξ_0 and π_0 are established through the first and second laws of thermodynamics. From the second law, the Clausius–Duhem inequality or dissipation inequality states that the dissipation is always non-negative. The local dissipation \mathcal{D}^{tot} at any material point in the reference configuration can be written as:

$$\mathcal{D}^{tot} = \int_{\Omega_0} [-\rho_0 \dot{\psi} + \mathbf{P} : \dot{\mathbf{F}} + \xi_0 \cdot \nabla_{\mathbf{X}} \dot{s} + \pi_0 \dot{s}] d\Omega_0 \geq 0 \quad (38)$$

The relation between the power-conjugation pairs of stress and strain-rate measures can be stated as:

$$\begin{aligned} \int_{\Omega_0} \mathbf{P} : \dot{\mathbf{F}} d\Omega_0 &= \int_{\Omega_0} \boldsymbol{\tau} : \mathbf{D} d\Omega_0 = \int_{\Omega_0} \boldsymbol{\tau} : \mathbf{L} d\Omega_0 = \int_{\Omega_0} \boldsymbol{\tau} : (\mathbf{L}^e + \mathbf{L}^p) d\Omega_0 \\ &= \int_{\Omega_0} \left(\boldsymbol{\tau} : \dot{\mathbf{F}}^e \mathbf{F}^{e-1} + \boldsymbol{\tau} : \mathbf{F}^e \mathbf{L}^p \mathbf{F}^{e-1} \right) d\Omega_0 = \int_{\Omega_0} \left(\boldsymbol{\tau} \mathbf{F}^{e-T} : \dot{\mathbf{F}}^e + \boldsymbol{\Xi} : \mathbf{L}^p \right) d\Omega_0 \\ &= \int_{\Omega_0} \left(\boldsymbol{\tau} \mathbf{F}^{e-T} : \dot{\mathbf{F}}^e + \sum_{\alpha}^N \tau^{\alpha} \dot{\gamma}^{\alpha} \right) d\Omega_0 \end{aligned} \quad (39)$$

$\mathbf{D} = \text{sym}(\mathbf{L})$ is the rate of deformation tensor. Then equation (38) can be rewritten as:

$$\int_{\Omega_0} \left[-\rho_0 \dot{\psi} + \boldsymbol{\tau} \mathbf{F}^{e-T} : \dot{\mathbf{F}}^e + \sum_{\alpha}^{N_{slip}} \tau^{\alpha} \dot{\gamma}^{\alpha} + \xi_0 \cdot \nabla_{\mathbf{X}} \dot{s} + \pi_0 \dot{s} \right] d\Omega_0 \geq 0 \quad (40)$$

Recall from Section 2.3 that the Helmholtz free energy density is a function of elastic deformation gradient \mathbf{F}^e , the defect internal state variables η^{α} ($= |\gamma^{\alpha}|$), the order parameter s and its gradient. Thus $\rho_0 \psi = \rho_0 \psi(\mathbf{F}^e, \eta^{\alpha} s, \nabla_{\mathbf{X}} s, \cdot)$. Applying chain rule to ψ , the dissipation inequality can be rearranged as:

$$\begin{aligned} \int_{\Omega_0} \left[\left(\boldsymbol{\tau} \mathbf{F}^{e-T} - \rho_0 \frac{\partial \psi}{\partial \mathbf{F}^e} \right) : \dot{\mathbf{F}}^e + \left(|\tau^{\alpha}| - \rho_0 \frac{\partial \psi}{\partial \eta^{\alpha}} \right) |\dot{\gamma}^{\alpha}| \right. \\ \left. + \left(\pi_0 - \rho_0 \frac{\partial \psi}{\partial s} \right) \dot{s} + \left(\xi_0 - \rho_0 \frac{\partial \psi}{\partial \nabla_{\mathbf{X}} s} \right) \cdot \nabla_{\mathbf{X}} \dot{s} \right] d\Omega_0 \geq 0 \end{aligned} \quad (41)$$

Since the non-negative dissipation should be valid for any combination of $(\dot{\mathbf{F}}^e, \dot{\gamma}^{\alpha}, \dot{s}, \nabla_{\mathbf{X}} \dot{s})$, each of the four terms in the LHS of Eq. (41) should be non-negative. Note that in the second term, the local plastic dissipation density $(|\tau^{\alpha}| - \rho_0 \frac{\partial \psi}{\partial \eta^{\alpha}}) |\dot{\gamma}^{\alpha}| = \tau^{\alpha} \dot{\gamma}^{\alpha} - g^{\alpha} |\dot{\gamma}^{\alpha}| = \mathcal{D}^p \geq 0$ has already been proved in Section 2.3.2. The remaining inequalities are:

$$\int_{\Omega_0} \left(\boldsymbol{\tau} \mathbf{F}^{e-T} - \rho_0 \frac{\partial \psi}{\partial \mathbf{F}^e} \right) d\Omega_0 \geq 0 \quad (42a)$$

$$\int_{\Omega_0} \left[\left(\pi_0 - \rho_0 \frac{\partial \psi}{\partial s} \right) \dot{s} + \left(\xi_0 - \rho_0 \frac{\partial \psi}{\partial \nabla_{\mathbf{X}} s} \right) \cdot \nabla_{\mathbf{X}} \dot{s} \right] d\Omega_0 \geq 0 \quad (42b)$$

Following developments in [51], Eq. (42a) leads to the finite deformation constitutive relations for the stress measure of the coupled mechanical-crack phase field problem as:

$$\boldsymbol{\tau} = \rho_0 \frac{\partial \psi}{\partial \mathbf{F}^e} \mathbf{F}^{eT} = \frac{1}{3} g_1 J^{e \frac{2}{3}} \left(\mathbf{I} : \mathbb{C}^e : \tilde{\mathbf{E}}^e \right) + g_2 \mathbf{F}^e \left(\mathbb{C}^e : \tilde{\mathbf{E}}^e \right) \mathbf{F}^{eT} \quad (43)$$

Next, the dissipation inequality for the crack phase field in Eq. (42b) may be written as:

$$\begin{aligned} \int_{\Omega_0} \left[\left(\pi_0 - \rho_0 \frac{\partial \psi}{\partial s} \right) \dot{s} + \left(\xi_0 - \rho_0 \frac{\partial \psi}{\partial \nabla_{\mathbf{X}} s} \right) \cdot \nabla_{\mathbf{X}} \dot{s} \right] d\Omega_0 = \\ \int_{\Omega_0} \left[\pi_0 - \rho_0 \frac{\partial \psi}{\partial s} - \nabla_{\mathbf{X}} \cdot \left(\xi_0 - \rho_0 \frac{\partial \psi}{\partial \nabla_{\mathbf{X}} s} \right) \right] \dot{s} d\Omega_0 + \int_{\Gamma_0} \left(\xi_0 - \rho_0 \frac{\partial \psi}{\partial \nabla_{\mathbf{X}} s} \right) \cdot \mathbf{N} \dot{s} d\Gamma_0 \geq 0 \end{aligned} \quad (44)$$

With a vanishing dissipation on the domain boundary, the internal micro-force is obtained as:

$$\xi_0 = \rho_0 \frac{\partial \psi}{\partial \nabla_{\mathbf{X}} s} \quad (45)$$

Therefore, the dissipation inequality for phase field variable in Eq. (44) is reduced to:

$$\int_{\Omega_0} \left(\pi_0 - \rho_0 \frac{\partial \psi}{\partial s} \right) \dot{s} d\Omega_0 \geq 0 \quad (46)$$

This equation can be enforced at every point as $\left(\pi_0 - \rho_0 \frac{\partial \psi}{\partial s} \right) \dot{s} \geq 0$. To ensure the satisfaction of the inequality, a viscosity term is artificially introduced in the crack phase field formulation by decomposing the internal micro-force π_0 into energetic π_0^{en} and dissipative π_0^{dis} components [50]. This is given as:

$$\pi_0 = \pi_0^{en} + \pi_0^{dis}, \quad \pi_0^{en} = \rho_0 \frac{\partial \psi}{\partial s} \quad \text{and} \quad \pi_0^{dis} = \beta_{gs} \dot{s} \quad (47)$$

Here β_{gs} is a non-negative viscous parameter. Setting $\beta_{gs} = 0$ renders the crack propagation rate-insensitive. Clearly, $\beta_{gs} \geq 0$ is a sufficient condition for the global inequality (46) and its local form to be satisfied.

2.5. Viscous stabilization to resolve convergence issues in the coupled model

In constitutive models with material degradation, instabilities can occur depending on the model geometry and constitutive parameters. When a part of the material is degraded, energy can be released from the neighboring sections undergoing localized deformation. Excess released energy can cause instability in the system, leading to non-equilibrium states. In these cases, static or quasi-static numerical solvers experience convergence issues [51]. Following [73], viscous stabilization has been used in [51] as an effective remedy for overcoming instabilities. This can be done at the local (constitutive model) and global (governing differential equation) levels. The artificial viscosity allows the system to dissipate excess energy and thus avoid instabilities. As in [51], the stress constitutive law is augmented by adding a viscosity term as:

$$\boldsymbol{\tau} = \frac{1}{3} g_1 J^{e \frac{2}{3}} \left(\mathbf{I} : \mathbb{C}^e : \tilde{\mathbf{E}}^e \right) + g_2 \mathbf{F}^e \left(\mathbb{C}^e : \tilde{\mathbf{E}}^e \right) \mathbf{F}^{eT} + \beta_{lu} \mathbf{F} \dot{\mathbf{E}} \mathbf{F}^T \quad (48)$$

where β_{lu} is a non-negative number representing local artificial viscosity for the displacement field.

A second approach for overcoming instabilities is the introduction of viscous forces in the governing differential equation of motion. This method has proved to be effective in modeling deformation of degradable materials [74]. Viscous forces are incorporated into the stress equilibrium equation as body forces, i.e.

$$\nabla_{\mathbf{X}} \cdot \mathbf{P} + \mathbf{B} - \beta_{gu} \dot{\mathbf{u}} = \mathbf{0} \quad \forall \mathbf{X} \in \Omega_0 \quad (49)$$

β_{gu} is the artificial global viscosity parameter for the displacement field. Viscous forces are assumed to be a linear function of velocity and their magnitudes are small for stable deformation. However, when a local region in the computational domain becomes unstable and nodal velocities increase drastically, the viscous forces play a key role in stabilizing the solution. As discussed in [74], β_{gu} may have spatial and temporal dependencies and can be adaptively modified for optimal performance. In this work, a linear dependence is assumed between the artificial global viscosity and the parameter s , i.e.

$$\beta_{gu} = \beta_{gu0} s \quad (50)$$

β_{gu0} is the reference global viscosity parameter. This treatment will ensure that the viscous stabilization is applied to regions in the computational domain, where material integrity is lost, i.e. regions where $s > 0$.

2.6. Summary of governing equations and constitutive relations

The governing differential equations, kinematic and kinetic equations and constitutive relations and kinetics laws in this section are summarized below.

$$\text{Equilibrium (Mechanical Field):} \quad \nabla_{\mathbf{X}} \cdot \mathbf{P} + \mathbf{B} - \beta_{gu} \dot{\mathbf{u}} = \mathbf{0} \quad \forall \mathbf{X} \in \Omega_0 \quad (51a)$$

$$\text{Equilibrium (Crack Phase):} \quad \nabla_{\mathbf{X}} \cdot \boldsymbol{\xi}_0 - \pi_0 = 0 \quad \forall \mathbf{X} \in \Omega_0 \quad (51b)$$

$$\begin{aligned} \text{Constitutive (Mechanical):} \quad \mathbf{P} = & \boldsymbol{\tau} \mathbf{F}^{-T} = \frac{1}{3} g_1 J^{e \frac{2}{3}} \left(\mathbf{I} : \mathbb{C}^e : \tilde{\mathbf{E}}^e \right) \mathbf{F}^{-T} \\ & + g_2 \mathbf{F}^e \left(\mathbb{C}^e : \tilde{\mathbf{E}}^e \right) \mathbf{F}^{p-T} + \beta \mathbf{F} \dot{\mathbf{E}} \end{aligned} \quad (51c)$$

$$\text{Crystal Plasticity: } \mathbf{L}^p = \dot{\mathbf{F}}^p \mathbf{F}^{p-1} = \sum_{\alpha=1}^{N_{slip}} \dot{\gamma}^\alpha \mathbf{m}_{0,slip}^\alpha \otimes \mathbf{n}_{0,slip}^\alpha \quad (51d)$$

$$\dot{\gamma}^\alpha = \dot{\gamma}_0^\alpha \left| \frac{\tau^\alpha}{g_0^\alpha + g^\alpha} \right|^{\frac{1}{m}} \text{sign}(\tau^\alpha) \quad (51e)$$

$$\dot{g}^\alpha = \sum_{\alpha}^{N_{slip}} h^{\alpha\beta} |\dot{\gamma}^\alpha| \quad (51f)$$

$$h^{\alpha\beta} = q^{\alpha\beta} h^\beta, \quad h^\beta = h_0^\beta \left| 1 - \frac{g^\beta}{g_s^\beta} \right|^r \text{sign} \left(1 - \frac{g^\beta}{g_s^\beta} \right),$$

$$g_s^\beta = \tilde{g} \left(\frac{\dot{\gamma}^\beta}{\dot{\gamma}} \right) \quad (51g)$$

$$\text{Constitutive (Crack Phase): } \xi_0 = \rho_0 \frac{\partial \psi}{\partial \nabla_{\mathbf{X}} s} = g_c l_c \nabla_{\mathbf{X}} s \quad (51h)$$

$$\pi_0 = \rho_0 \frac{\partial \psi}{\partial s} + \beta_{gs} \dot{s} = \rho_0 \frac{\partial \psi^e}{\partial s} + \rho_0 \frac{\partial \psi^d}{\partial s} + \rho_0 \frac{\partial \psi^c}{\partial s} + \beta_{gs} \dot{s} \quad (51i)$$

$$\frac{\partial \psi^e}{\partial s} = \left(\hat{\mathbf{E}}^e : \mathbb{C}^e : \hat{\mathbf{E}}^e \right)_s + \mathbf{E}^e : \mathbb{C}^e : \hat{\mathbf{E}}^e \quad \text{where}$$

$$\hat{\mathbf{E}}^e = \frac{\tilde{\mathbf{E}}^e}{\partial s} = \left[-\mathcal{H}(J^e - 1) (1 - \kappa_s) \mathbf{E}_{vol}^e - (1 - \kappa_s) \mathbf{E}^e \right] \quad (51j)$$

$$\frac{\partial \psi^d}{\partial s} = -\frac{1}{2} \sum_{\alpha, \beta}^{N_{slip}} h^{\alpha\beta} |\dot{\gamma}^\alpha| |\dot{\gamma}^\beta| \quad (51k)$$

$$\frac{\partial \psi^c}{\partial s} = \frac{g_c}{l_c} s \quad (51l)$$

$$\text{Traction Reciprocity: } \mathbf{T} = \mathbf{P} \mathbf{N} \quad \forall \mathbf{X} \in \Gamma_{0T}, \quad \lambda_0 = \xi_0 \cdot \mathbf{N} \quad \forall \mathbf{X} \in \Gamma_{0\lambda} \quad (51m)$$

$$\text{Dirichlet BC: } \mathbf{u} = \bar{\mathbf{u}} \quad \text{on } \Gamma_{0u}, \quad s = \bar{s} \quad \text{on } \Gamma_{0s} \quad (51n)$$

Note that in Eq. (51b), the microscopic body force $l_0 (= 0)$ for crack phase field is set to zero, since it does not connect to a physical quantity in this context.

3. Finite element formulation and implementation of the coupled crystal plasticity-phase field model

Governing equations, constitutive relations and boundary conditions for the displacement and crack phase fields are coupled in Eqs. (51a) to (51n), as they are derived from the Helmholtz free energy density that is a function of both the displacements \mathbf{u} and order parameter s . Finite element weak forms are developed by applying the method of weighted residuals to equation sets that are consolidated from (51a) to (51n), to yield the principle of virtual power for the mechanical and phase problems. The weak forms for the coupled crystal plasticity-crack phase field problem are expressed as:

$$\text{Mechanical: } \int_{\Omega_0} \mathbf{P} : \delta \mathbf{F} d\Omega_0 = \int_{\Gamma_{0T}} \mathbf{T} \cdot \delta \mathbf{u} d\Gamma_{0T} + \int_{\Omega_0} \mathbf{B} \cdot \delta \mathbf{u} d\Omega_0 - \int_{\Omega_0} \beta_{gu} \dot{\mathbf{u}} \cdot \delta \mathbf{u} d\Omega_0 \quad (52a)$$

$$\text{Phase Field: } \int_{\Omega_0} g_c l_c \nabla_{\mathbf{X}} s \cdot \nabla_{\mathbf{X}} \delta s d\Omega_0 + \int_{\Omega_0} s \left[\frac{g_c}{l_c} + \hat{\mathbf{E}}^e : \mathbb{C}^e : \hat{\mathbf{E}}^e \right] \delta s d\Omega_0 = \int_{\Gamma_{0\lambda}} \lambda_0 \delta s d\Gamma_{0\lambda} + \int_{\Omega_0} \left[-\mathbf{E}^e : \mathbb{C}^e : \hat{\mathbf{E}}^e + \frac{1}{2} \sum_{\alpha, \beta} h^{\alpha\beta} |\dot{\gamma}^\alpha| |\dot{\gamma}^\beta| - \beta_{gs} \dot{s} \right] \delta s d\Omega_0 \quad (52b)$$

Eqs. (52a) and (52b) are respectively the weak forms for the mechanical field and crack phase field, expressed in the reference configuration. A total Lagrangian formulation, corresponding to the fixed reference configuration is adopted. It expedites finite element computations of the phase field problem, by avoiding repeated evaluation

of configuration-dependent matrices such as the shape function gradient matrix, in each increment of the solution process.

3.1. Numerical implementation in finite element models

Finite element solutions of the coupled mechanical-crack phase field model have been developed in [23,50,75]. Crystal plasticity FE models of polycrystalline microstructures, e.g. in [41,42] have conventionally used four-noded tetrahedron (TET4) elements to discretize the computational domain Ω . A locking-free, stabilized finite element formulation has been developed for TET4 elements applied to crystal plasticity problems with incompressibility constraints in [76]. In the present analysis of the coupled problem, the same mesh and shape functions are used to interpolate the displacement and the phase field variables, i.e.

$$\mathbf{u}^h(\mathbf{X}) = \sum_{\beta}^{N_{nodes}} \mathbf{u}_{\beta} N_{\beta}(\mathbf{X}) \quad \text{and} \quad s^h(\mathbf{X}) = \sum_{\beta}^{N_{nodes}} s_{\beta} N_{\beta}(\mathbf{X}) \quad \forall \Omega_e, e = 1, \dots, n_{elem} \quad (53)$$

where N_{β} is the finite element shape function associated with a node β , and $\mathbf{u}_{\beta} = [u_{X\beta}, u_{Y\beta}, u_{Z\beta}]$ and s^{β} are the nodal values of displacement components and phase field parameter. Their spatial gradients in the reference coordinates are approximated as:

$$\begin{aligned} \nabla_{\mathbf{X}} \mathbf{u}^h(\mathbf{X}) &= \sum_{\beta}^{N_{nodes}} \mathbf{u}_{\beta} \otimes \nabla_{\mathbf{X}} N_{\beta}(\mathbf{X}) = [\mathbf{G}^u] \{\mathbf{u}\} \quad \text{and} \\ \nabla_{\mathbf{X}} s^h(\mathbf{X}) &= \sum_{\beta}^{N_{nodes}} s_{\beta} \nabla_{\mathbf{X}} N_{\beta}(\mathbf{X}) = [\mathbf{G}^s] \{s\} \quad \forall \Omega_e, e = 1, \dots, n_{elem} \end{aligned} \quad (54)$$

where $[\mathbf{G}^u]$ and $[\mathbf{G}^s]$ are the gradient matrices for the displacement field and phase field parameter in the reference configuration. Henceforth, the subscript $_X$ on all gradient terms will be omitted and imply spatial derivatives with respect to the reference coordinates. $\{\Delta \mathbf{u}\}$ and $\{\Delta s\}$ are arrays of nodal displacements and phase field parameter respectively.

3.1.1. Solution strategy for the nonlinear coupled problem

Simultaneous solution of the coupled system for displacement and phase-field degrees of freedom using monolithic solvers can lead to ill-conditioning and lack of convergence. The energy functional corresponding to PFM is typically non-convex in (\mathbf{u}, s) [54]. Stiffness matrix components for the coupled system can be orders of magnitude different, corresponding to displacement and order parameter degrees of freedom (DOFs). The staggered solution scheme on the other hand, where each governing equation is solved for one of the fields while keeping the other field fixed, is a preferred choice since the energy functional is convex w.r.t. each of \mathbf{u} and s individually. Over-relaxation and line search techniques have been applied recently to improve the performance of staggered [75] solvers.

An incremental finite element analysis is conducted, where variables at the discrete at time $t + \Delta t$ are solved from a set of linearized nonlinear equations, with known displacement and crack phase-field variables at time t . For an increment $\Delta t = t \rightarrow t + \Delta t$, the finite element discretized weak form is obtained by applying equations (53) and (54) to the weak form of Eq. (52) and applying the backward Euler time integration scheme. The resulting discretized finite element weak forms are:

$$\begin{aligned} \text{Mechanical Field: } [\mathbf{K}_u]^t \{\Delta \mathbf{u}\} &= \{\mathbf{f}_u^{ext}\}^{t+\Delta t} - \{\mathbf{f}_u^{int}\}^t \quad \text{where} \\ [\mathbf{K}_u]^t &= \sum_e^{N_{elem}} \left[[\mathbf{G}^u]^T : \mathbb{A}^t : [\mathbf{G}^u] + \frac{\beta_{gu}}{\Delta t} [\mathbf{N}^u]^T [\mathbf{N}^u] \right] \Omega_0^e \\ \{\mathbf{f}_u^{ext}\}^{t+\Delta t} &= \sum_e^{N_{elem}} [\mathbf{N}^u]^T \mathbf{T}^{t+\Delta t} \Gamma_{0T}^e + \sum_e^{N_{elem}} [\mathbf{N}^u]^T \mathbf{B}^{t+\Delta t} \Omega_0^e \\ \{\mathbf{f}_u^{int}\}^t &= \sum_e^{N_{elem}} [\mathbf{G}^u]^T \mathbf{P}^t \Omega_0^e \end{aligned} \quad (55)$$

Phase Field: $[\mathbf{K}_s]^t \{\Delta s\} = \{\mathbf{f}_s^{ext}\}^{t+\Delta t} - \{\mathbf{f}_s^{int}\}^t$ where

$$[\mathbf{K}_s]^t = \sum_e^{N_{elem}} \left[g_c l_c [\mathbf{G}^s]^T [\mathbf{G}^s] + \left(\frac{g_c}{l_c} + \hat{\mathbf{E}}^{e,t} : \mathbb{C}^e : \hat{\mathbf{E}}^{e,t} + \frac{\beta_{gs}}{\Delta t} \right) [\mathbf{N}^s]^T [\mathbf{N}^s] \right] \Omega_0^e$$

$$\{\mathbf{f}_s^{ext}\}^{t+\Delta t} = \sum_e^{N_{elem}} [\mathbf{N}^s]^T \lambda_0^{t+\Delta t} \Gamma_{0\lambda}^e$$

$$\{\mathbf{f}_s^{int}\}^t = \sum_e^{N_{elem}} \left[g_c l_c [\mathbf{G}^s]^T [\mathbf{G}^s] + \left(\frac{g_c}{l_c} + \hat{\mathbf{E}}^{e,t} : \mathbb{C}^e : \hat{\mathbf{E}}^{e,t} \right) [\mathbf{N}^s]^T [\mathbf{N}^s] \right] \Omega_0^e \{s\}^t$$

$$- \sum_e^{N_{elem}} [\mathbf{N}^s]^T \left[-\mathbf{E}^{e,t} : \mathbb{C}^e : \hat{\mathbf{E}}^{e,t} + \frac{1}{2} \sum_{\alpha,\beta} h^{\alpha\beta} |\gamma^\alpha|^t |\gamma^\beta|^t \right] \Omega_0^e$$

Here $\mathbb{A} = \partial \mathbf{P} / \partial \mathbf{F}$ is the material stiffness tensor. $[\mathbf{K}_u]$, $\{\mathbf{f}_u^{ext}\}$, $\{\mathbf{f}_u^{int}\}$, $[\mathbf{K}_s]$, $\{\mathbf{f}_s^{ext}\}$, $\{\mathbf{f}_s^{int}\}$ are the global stiffness matrix, global external and internal force vectors for displacement field and phase field, respectively. The superscript $t + \Delta t$ and t indicate discrete time points in the incremental process.

In the staggered solution algorithm for the coupled FE problem in Eqs. (55) and (56), the nonlinear displacement problem is solved first with fixed phase field variables. The elastic and defect energy densities are derived from this solution, which drives crack propagation through the phase field surface energy. Subsequently the phase field evolution problem is solved with fixed mechanical field variables. The solution process iterates between the phase field and mechanical field problems until the convergence is achieved for both fields, before proceeding to the next increment. The nonlinear finite element problem for displacements is iteratively solved by the Newton–Raphson algorithm. The nodal displacement in the $(i + 1) - th$ iteration $\{\Delta \mathbf{u}\}_{i+1}$ is expressed as:

$$\{\Delta \mathbf{u}\}_{i+1} = \{\Delta \mathbf{u}\}_i + \{\mathbf{d}_u\} \quad (57)$$

where $\{\mathbf{d}_u\}$ is the correction to the nodal displacement increment at iteration i , obtained by solving the equation:

$$[\mathbf{K}_u]_i^{t+\Delta t} \{\mathbf{d}_u\} = \{\mathbf{f}_u^{ext}\}^{t+\Delta t} - \{\mathbf{f}_u^{int}\}_i^{t+\Delta t} - \sum_e^{N_{elem}} \beta_{gu} \frac{\{\Delta \mathbf{u}\}_i}{\Delta t} [\mathbf{N}^u]^T [\mathbf{N}^u] \Omega_0^e \quad (58)$$

Upon convergence of the displacement solution, the mechanical driving force for crack propagation in Eq. (51i) is passed to the phase field problem given by Eq. (56). The phase field parameter in the $(j + 1)th$ iteration is updated as:

$$\{\Delta s\}_{j+1} = \{\Delta s\}_j + \{d_s\} \quad (59)$$

where $\{d_s\}$ is the iterative correction to the incremental phase field parameter at the $i - th$ iteration. Applying this relation to Eq. (56), the phase field parameter update $\{d_s\}$ in the staggered iteration process of increment $\Delta t = t \rightarrow t + \Delta t$ is obtained as:

$$[\mathbf{K}_s]_j^{t+\Delta t} \{d_s\} = \{\mathbf{f}_s^{ext}\}^{t+\Delta t} - \{\mathbf{f}_s^{int}\}_j^{t+\Delta t} - \sum_e^{N_{elem}} \beta_{gs} \frac{\{\Delta s\}_j}{\Delta t} [\mathbf{N}^s]^T [\mathbf{N}^s] \Omega_0^e \quad (60)$$

The iteration stops when the phase field parameter converges with $\|\{d_s\}\| \leq \zeta$, where ζ is a very small number.

3.1.2. Enforcing fracture irreversibility

In the absence of crack healing (not considered in this study), the unilateral condition of crack closure [70] is governed by the condition $\dot{s} \geq 0$. This corresponds to the tension–compression asymmetry based formulation of the degradable elastic energy discussed in Section 2.3.1. In the numerical model, the condition $\dot{s} \geq 0$ does not guarantee irreversibility in crack opening conditions, as this could be satisfied during unloading as well. An effective solution has been proposed in [77], where the local history of the maximum positive energy density is introduced to enforce irreversibility. A positive energy density corresponds to the part of the Helmholtz free energy density

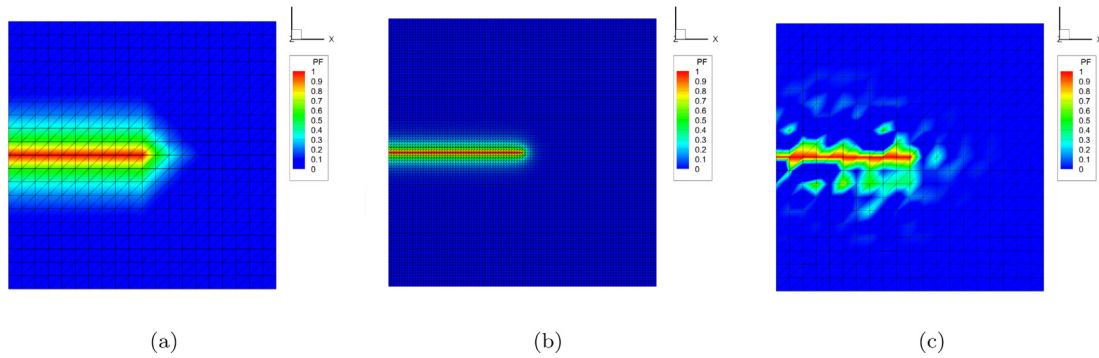


Fig. 2. Contour plots of simulated crack phase field parameter using different TET4 element sizes and length-scale parameters l_c : (a) coarse mesh of element size $5 \mu\text{m}$ and $l_c = 10 \mu\text{m}$, (b) fine mesh of element size $1 \mu\text{m}$ and $l_c = 2 \mu\text{m}$, and (c) coarse mesh of element size $5 \mu\text{m}$ and $l_c = 2 \mu\text{m}$.

that is degraded by the crack phase field. It drives the evolution of phase field order parameter s . Decrease in the positive energy density will cause a reduction in s . Thus, by storing the temporally maximum value of the local positive energy density as a state variable at a given material point, the non-negativeness of \dot{s} can be assured. A similar approach is adopted in this work in the context of crystal plasticity, to enforce the irreversibility of crack opening. Combining equations (51h), (51i) and (51b), one obtains:

$$\beta_{gs}\dot{s} = -\rho_0 \frac{\partial \psi^e}{\partial s} - \rho_0 \frac{\partial \psi^d}{\partial s} - \frac{g_c}{l_c} (s - l_c^2 \nabla_{\mathbf{X}} \cdot \nabla_{\mathbf{X}} s) \quad (61)$$

This is the strong form of the phase field problem. The term $(f_{mech} = \rho_0 \frac{\partial \psi^e}{\partial s} + \rho_0 \frac{\partial \psi^d}{\partial s})$ is the mechanical driving force from elastic deformation and defects. The condition $\dot{f}_{mech}(\mathbf{X}) \geq 0$ corresponds to $\dot{s}(\mathbf{X}) \geq 0$. Hence, crack irreversibility is enforced by replacing $f_{mech}(\mathbf{X})$ with $\max_{[0, t+\Delta t]} f_{mech}(\mathbf{X})$ in Eq. (51i).

4. Wavelet-enriched adaptive hierarchical FE model for high resolution phase-field analysis

4.1. Mesh dependence of the coupled CPFE-phase field model

As discussed in the introduction, finite element implementation of the crack phase field model faces major difficulties from the required mesh resolution. The mesh has to be highly refined to resolve the critical phase field length-scale parameter l_c for simulating the sharp crack. The effect of mesh resolution is illustrated in Fig. 2 with two different mesh sizes and two l_c 's to represent a crack.

The size of the 3D computational model in Fig. 2 is set to $100 \mu\text{m} \times 100 \mu\text{m} \times 1 \mu\text{m}$. An initial through thickness ($0 \mu\text{m} \leq z \leq 1 \mu\text{m}$) sharp crack is created along the surface $0 \mu\text{m} \leq x \leq 50 \mu\text{m}$, $y = 50 \mu\text{m}$ by setting the nodal phase field value to $s = 1$ as the initial condition. No external mechanical load is applied to the model. The model is run for one relaxation step to capture the phase field representation of the sharp crack. Fig. 2(a) shows the result with a coarse TET4 mesh of element size $h = 5 \mu\text{m}$ and a high characteristic length-scale parameter $l_c = 10 \mu\text{m}$. The phase field solution shows a diffused representation of the crack due to the large value of l_c . In contrast, the fine mesh model with TET4 element size $h = 1 \mu\text{m}$ in Fig. 2(b) with a small $l_c = 2 \mu\text{m}$, depicts a sharp crack. Clearly, a sharp crack topology requires high mesh resolution and a small length-scale parameter. Non-physical solutions may arise from using a coarse mesh with a small value of l_c , as shown in Fig. 2(c). In this simulation, the TET4 element size is $h = 5 \mu\text{m}$ and $l_c = 2 \mu\text{m}$. Results show crack blunting and non-physical diffusion of the order parameter. For 3D crystal plasticity simulations, typical mesh size is an order or two higher than that required for crack representation with a small l_c value. Simulations become infeasible if the entire crystal plasticity model has to be reduced to the mesh size needed for crack modeling, due to extreme requirements of memory and computing time. This is addressed in this section through a wavelet-enriched adaptive hierarchical finite element model.

4.2. Wavelet-enriched adaptive hierarchical FE model

The *wavelet-enriched adaptive hierarchical FE model* or (WAHFEM) has been developed to solve elastic problems in [61] and crystal plasticity problem [62]. The method adaptively creates an optimal discretization space conforming to the solution profile by projecting the solution field onto a set of scaling and multi-resolution wavelet basis functions. The methods have shown superior convergence rate and significant reduction in computation time in comparison with conventional polynomial based hierarchical methods [61,62]. This section extends the WAHFEM to the solve the coupled mechanical-phase field problem. The concept of adaptive hierarchical FEM is briefly discussed followed by the integration of wavelet basis functions for hierarchical enrichment of both the mechanical and phase field problems.

4.2.1. Hierarchical enrichment of coupled mechanical and phase field FE model

Most finite element formulations are built on the mathematical foundation of partition of unity. Consequently, adaptive strategies that either invoke mesh refinement (h-adaptation) and/or basis function enrichment (p-adaptation) discard or modify the initial discretization space. Mesh enhancement strategy in many of the above methods does not guarantee conformity of the new enriched space to the solution profile. The hierarchical finite element basis is composed of a set of standard finite element shape functions and a set of hierarchical enrichment functions. The latter functions do not necessarily admit partition of unity. The basis of hierarchical functions does not constitute an interpolation basis, and enrichment function degrees of freedom are associated with displacement correction rather than displacement values. This type of functions preserves the initial discretization space and expand it into a enriched space during the adaptation process. Multi-scale hierarchical enrichment can lead to a significant enhancement of convergence rates and matrix conditioning [78].

A hierarchical algorithm is proposed for the coupled mechanical-phase field finite element model. For a time increment $\Delta t = t \rightarrow t + \Delta t$, the adaptive enhancement finds the optimal discretization space $V^{h(t+\Delta t)}(\Omega)$ for both the displacement and phase field parameter fields that will reduce the discretization errors on both fields to within a prescribed tolerance. As in Section 3.1, the same mesh and basis functions are used for the displacement and phase field, i.e. $V^h(\Omega)_{\mathbf{u}} = V^h(\Omega)_s = V^h(\Omega)$. Assume that the approximate solutions of the \mathbf{u} and s fields at time t are evaluated on the discretized space $V^{h(t)}(\Omega) \subset V(\Omega)$:

$$\mathbf{u}^h(\mathbf{X}) = \sum_{\beta}^m \mathbf{u}_{\beta}^h N_{\beta}(\mathbf{X}) + \sum_{\eta}^{m_{enr(t)}} \mathbf{w}_{\eta}^{\mathbf{u},h} \varphi_{\eta}^t(\mathbf{X}) \quad \forall \mathbf{X} \in \Omega_0 \quad (62a)$$

$$s^h(\mathbf{X}) = \sum_{\beta}^m s_{\beta}^h N_{\beta}(\mathbf{X}) + \sum_{\eta}^{m_{enr(t)}} w_{\eta}^{s,h} \varphi_{\eta}^t(\mathbf{X}) \quad \forall \mathbf{X} \in \Omega_0 \quad (62b)$$

where the same shape function N_{β} and hierarchical enrichment function φ_{η}^t are used for both the displacement and phase field solutions. The family $\{N\}^m$ of m shape functions N_{β} corresponds to the interpolation of \mathbf{u} in the original coarse finite element discretization space at the initial time $t = 0$. Hence m is the number of nodes in the original coarse mesh of the domain Ω_0 . The set $\{N\}^m$ of standard finite element basis functions admits partition of unity. The family $\{\varphi\}^{m_{enr(t)}}$ corresponds to the set of hierarchical enrichment functions at time t that do not necessarily admit partition of unity. \mathbf{u}_{β}^h and s_{β}^h are respectively the displacement components and phase field parameter at node β , $\mathbf{w}_{\eta}^{\mathbf{u},h}$ and $w_{\eta}^{s,h}$ are the coefficients associated with hierarchical enrichment functions. The latter is interpreted as the corrections to coarse finite element solutions at an enrichment node η . The adaptive method introduces a set of enrichment functions $\{\varphi\}^{m_{enr}}$ in the hierarchy, which expand the discretization space $V^h(\Omega)$ to an enriched space $V^{h_{enr}}(\Omega) \supset V^h(\Omega)$, while preserving the original set of discretization functions $\{N\}^m$. $m_{enr(t)}$ corresponds to number of additional enrichment nodes that are hierarchically added to the initial mesh.

Assume the set $\{\phi\}^n$ is an arbitrarily large ($n \rightarrow \infty$) and sufficient set of multi-scale hierarchical enrichment functions for the coarse discretization space $\{N\}^m$. The functions in the set $\{\phi\}^n$ are the standard C^0 hierarchical FEM shape functions obtained by uniform subdivision of the coarse mesh [61]. For the time increment $\Delta t = t \rightarrow t + \Delta t$, the adaptive method finds an optimal set $\{\varphi\}^{m_{enr(t+\Delta t)}} \subset \{\phi\}^n$ such that:

$$\|\mathbf{u} - \mathbf{u}^{h_{enr}}\| \leq \epsilon_{\mathbf{u}} \quad \text{and} \quad \|s - s^{h_{enr}}\| \leq \epsilon_s \quad (63)$$

where

$$\mathbf{u}^{h_{enr}}(\mathbf{X}) = \sum_{\beta}^m \mathbf{u}_{\beta}^{h_{enr}} N_{\beta}(\mathbf{X}) + \sum_{\eta}^{m_{enr}(t+\Delta t)} \mathbf{w}_{\eta}^{\mathbf{u}, h_{enr}} \varphi_{\eta}^{t+\Delta t}(\mathbf{X}) \quad \forall \mathbf{X} \in \Omega_0 \quad (64a)$$

$$s^{h_{enr}}(\mathbf{X}) = \sum_{\beta}^m s_{\beta}^{h_{enr}} N_{\beta}(\mathbf{X}) + \sum_{\eta}^{m_{enr}(t+\Delta t)} w_{\eta}^{s, h_{enr}} \varphi_{\eta}^{t+\Delta t}(\mathbf{X}) \quad \forall \mathbf{X} \in \Omega_0 \quad (64b)$$

The enrichment algorithm has been detailed in [62] for crystal plasticity analysis of a polycrystalline model. The algorithm starts with an initial guess for the displacement $\mathbf{u}^{h(t+\Delta t)}$ at time $t + \Delta t$, using the converged set of basis functions $\{N_1 \dots N_m, \varphi_1^t, \dots, \varphi_{m_{enr}(t)}^t\}$ at time t . Subsequently, $\mathbf{u}^{h(t+\Delta t)}$ is projected to next higher scale of hierarchical enrichment functions using a modified Jacobi method to find a new optimal enrichment basis for time $t + \Delta t$ as detailed in [62]. This algorithm works well for the crystal plasticity problem alone. However as shown in Section 4.1, the coupled mechanical-phase field solution based on an inadequate discretization space has significant errors and is unreliable. For this problem, the converged discretization space $V^{h(t)} = span\{N_1 \dots N_m, \varphi_1^t, \dots, \varphi_{m_{enr}(t)}^t\}$ at time t does not guarantee a sufficiently fine resolution for the propagated crack at time $t + \Delta t$. The modified Jacobi method-based algorithm in [62] is not deemed suitable for the coupled mechanical-phase field fracture problem.

4.2.2. Enrichment algorithm based on static condensation

A static condensation method based enrichment algorithm is proposed as a remedy to the above deficiency. The algorithm first defines a sufficiently high resolution discretization space at time $t + \Delta t$ by adding new hierarchical enrichment functions $\{\phi\}^p$ to the existing basis $\{\varphi\}^{m_{enr}(t)}$. Subsequently, the corresponding hierarchical FE stiffness matrix and residuals for the increment $\Delta t = t \rightarrow t + \Delta t$ are computed for both mechanical field and phase field problems and condensed onto the $m + m_{enr}(t)$ nodes, respectively. The solution is estimated using a modified static condensation method, from which the optimal enrichment functions $\{\varphi\}^{m_{enr}(t+\Delta t)}$ are determined. The solution estimate using this method takes into account the effect of new enrichment functions $\{\phi\}^p$. The modified static condensation method makes the algorithm computationally efficient. For the subsequent staggered Newton–Raphson nonlinear solution of the coupled problems for this time increment, the function $\{\varphi\}^{m_{enr}(t+\Delta t)}$ is not updated further. A flowchart of the solution algorithm for the time step $t \rightarrow \Delta t$ is summarized in Fig. 3. The enrichment algorithm that determines $\{\varphi\}^{m_{enr}(t+\Delta t)}$ is described next.

- **Step 1- Initialize:** Define a basis $\{\phi\}^p \subset \{\phi\}^n$ with higher resolution hierarchical enrichment functions, on which the displacement and phase field estimates $\tilde{\mathbf{u}}$ and \tilde{s} are sought. The initial discretization basis for evaluating the solution estimate $\tilde{\mathbf{u}}$ and \tilde{s} is expressed as $\{N\}^m \cup \{\varphi\}_{(0)}^{m_{enr}(t+\Delta t)} \cup \{\phi\}^p$, where:

$$\{\varphi\}_{(0)}^{m_{enr}(t+\Delta t)} = \{\varphi\}^{m_{enr}(t)} \quad (65)$$

- **Step 2: Update enrichment basis:** For a iteration step $(k + 1)$

- Compute the solution estimate $\tilde{\mathbf{u}}$ and \tilde{s} by solving equation (52) on the discretization basis $\{N\}^m \cup \{\varphi\}_{(k)}^{m_{enr}(t+\Delta t)} \cup \{\phi\}^p$. This is done using modified static condensation method as described in Section 4.2.3.
- Select the new enrichment basis $\{\varphi\}_{(k+1)}^{m_{enr}(t+\Delta t)}$.
 - * Identify a minimal set $\{\varphi\}_{(k+1)}^{m_{enr}(t+\Delta t), \mathbf{u}} \subset \{\varphi\}_{(k)}^{m_{enr}(t+\Delta t)} \cup \{\phi\}^p$, such that the projection $P(\tilde{\mathbf{u}})$ of $\tilde{\mathbf{u}}$ on $\{N\}^m \cup \{\varphi\}_{(k+1)}^{m_{enr}(t+\Delta t)}$ admits the inequality to within a given tolerance $\zeta^{\mathbf{u}}$, written as:

$$\|P(\tilde{\mathbf{u}}) - \tilde{\mathbf{u}}\| \leq \zeta^{\mathbf{u}} \quad (66)$$

- * Identify a minimal set $\{\varphi\}_{(k+1)}^{m_{enr}(t+\Delta t), s} \subset \{\varphi\}_{(k)}^{m_{enr}(t+\Delta t)} \cup \{\phi\}^p$, such that the projection $P(\tilde{s})$ of \tilde{s} on $\{N\}^m \cup \{\varphi\}_{(k+1)}^{m_{enr}(t+\Delta t)}$ admits the inequality to within a given tolerance ζ^s , written as:

$$\|P(\tilde{s}) - \tilde{s}\| \leq \zeta^s \quad (67)$$

- * The new enrichment basis $\{\varphi\}_{(k+1)}^{m_{enr}(t+\Delta t)}$ is then selected as:

$$\{\varphi\}_{(k+1)}^{m_{enr}(t+\Delta t)} = \{\varphi\}_{(k+1)}^{m_{enr}(t+\Delta t), \mathbf{u}} \cup \{\varphi\}_{(k+1)}^{m_{enr}(t+\Delta t), s} \quad (68)$$

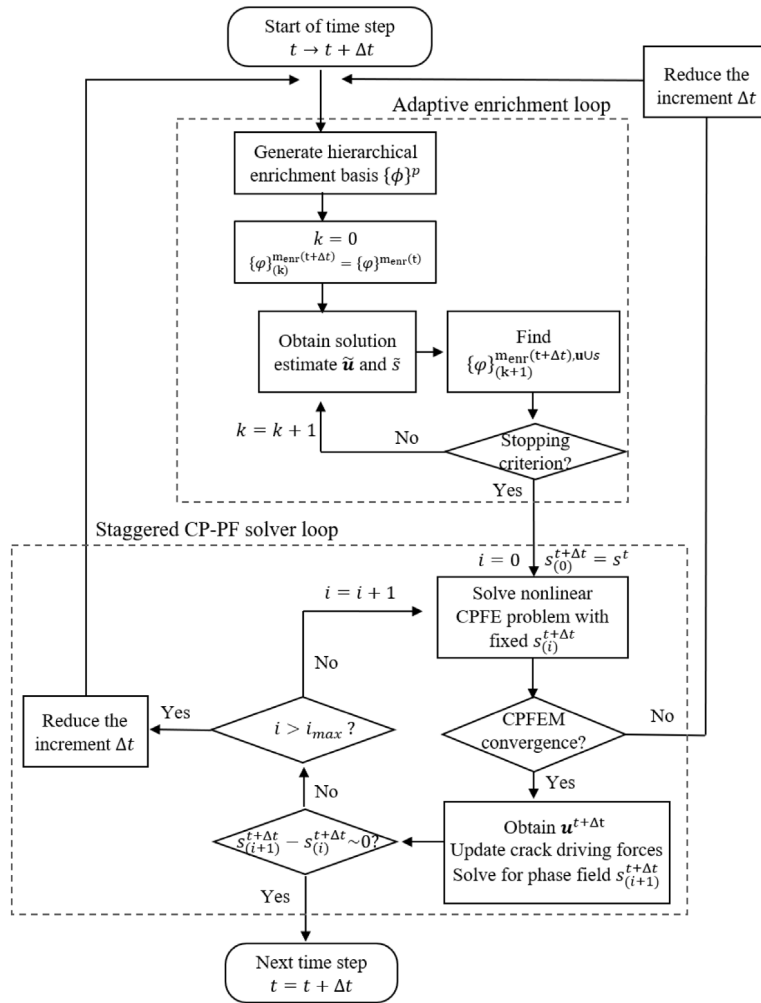


Fig. 3. Flowchart showing the schematic of adaptive, hierarchical crystal plasticity-phase field finite element model.

• **Step 3: Stop:** Following the convergence criterion, terminate iteration if:

$$\exists j \leq k \mid \{\varphi\}_{(k+1)}^{m_{enr}(t+\Delta t)} = \{\varphi\}_{(j)}^{m_{enr}(t+\Delta t)} \quad (69)$$

4.2.3. Static condensation method for computing the solution estimates $\tilde{\mathbf{u}}$ and $\tilde{\mathbf{s}}$

Due to the stringent requirements of discretization resolution of the coupled mechanical-phase field problem, the solution estimate $\tilde{\mathbf{u}}$ and $\tilde{\mathbf{s}}$ should be directly computed with the enhanced interpolation basis $\{N\}^m \cup \{\varphi\}_{(k)}^{m_{enr}(t+\Delta t)} \cup \{\phi\}^p$. A computationally efficient estimation method is proposed here based on a modified static condensation technique. For the $k+1$ -th iteration, the interpolation of $\tilde{\mathbf{u}}_{(k)}$ and $\tilde{\mathbf{s}}_{(k)}$ is given by:

$$\tilde{\mathbf{u}}_{(k)}(\mathbf{X}) = \sum_{\beta}^{m+m_{enr}(t+\Delta t)} \hat{\mathbf{u}}^* \hat{N}_{\beta(k)}(\mathbf{X}) + \sum_{\beta}^p \mathbf{q}_{\beta}^u \phi_{\beta}(\mathbf{X}) \quad (70a)$$

$$\tilde{\mathbf{s}}_{(k)}(\mathbf{X}) = \sum_{\beta}^{m+m_{enr}(t+\Delta t)} \hat{\mathbf{s}}^* \hat{N}_{\beta(k)}(\mathbf{X}) + \sum_{\beta}^p q_{\beta}^s \phi_{\beta}(\mathbf{X}) \quad (70b)$$

where

$$\sum_{\alpha}^{m+m_{enr}(t+\Delta t)} \hat{\mathbf{u}}^* \hat{N}_{\alpha(k)}(\mathbf{X}) = \sum_{\alpha}^m \hat{\mathbf{u}}_{\alpha} N_{\alpha}(\mathbf{X}) + \sum_{\gamma}^{m_{enr}(t+\Delta t)} \hat{\mathbf{w}}_{\gamma}^{\mathbf{u},h_{enr}} \varphi_{\gamma(k)}^{t+\Delta t}(\mathbf{X}) \quad (71a)$$

$$\sum_{\alpha}^{m+m_{enr}(t+\Delta t)} \hat{s}^* \hat{N}_{\alpha(k)}(\mathbf{X}) = \sum_{\alpha}^m \hat{s}_{\alpha} N_{\alpha}(\mathbf{X}) + \sum_{\gamma}^{m_{enr}(t+\Delta t)} \hat{w}_{\gamma}^{s,h_{enr}} \varphi_{\gamma(k)}^{t+\Delta t}(\mathbf{X}) \quad (71b)$$

Note that here $\{\hat{N}_{(k)}\}$ represents the converged shape functions at iteration k . $\{\hat{\mathbf{u}}^*\}$ and $\{\hat{s}^*\}$ are solution estimates associated with $\{\hat{N}_{(k)}\}$ that should be solved. $\{\mathbf{q}^{\mathbf{u}}\}$ and $\{q^s\}$ are the remainder of the solution estimates to be solved, associated with the potential refinement basis $\{\phi\}^p$. The discretized gradients $\nabla(\tilde{\mathbf{u}})$ and $\nabla(\tilde{s})$ can be obtained from Eq. (70) and are expressed as:

$$\nabla(\tilde{\mathbf{u}}) = [\mathbf{G}_{(k)}^{\mathbf{u}}] \{\hat{\mathbf{u}}^*\} + [\Theta^{\mathbf{u}}] \{\mathbf{q}^{\mathbf{u}}\} \quad (72a)$$

$$\nabla(\tilde{s}) = [\mathbf{G}_{(k)}^s] \{\hat{s}^*\} + [\Theta^s] \{q^s\} \quad (72b)$$

$[\mathbf{G}_{(k)}^{\mathbf{u}}]$ and $[\mathbf{G}_{(k)}^s]$ correspond to the gradient matrices associated with the interpolation functions $\{\hat{N}_{(k)}\}^{m+m_{enr}(t+\Delta t)}$, while $[\Theta^{\mathbf{u}}]$ and $[\Theta^s]$ are the gradient matrices associated with $\{\phi\}^p$. The linearized finite element equations for solving for the estimates $\Delta\tilde{\mathbf{u}} (= \tilde{\mathbf{u}} - \mathbf{u}_t)$ and $\Delta\tilde{s} (= \tilde{s} - s_t)$ are obtained by substituting Eqs. (70) and (72) into Eq. (52). The mechanical part of the resulting matrix equations is written as:

$$\begin{bmatrix} [\mathbf{K}_{(k)}^{\mathbf{u}}] & [\mathbf{C}^{\mathbf{u}}]^T \\ [\mathbf{C}^{\mathbf{u}}] & [\mathbf{A}^{\mathbf{u}}] \end{bmatrix} \begin{Bmatrix} \{\Delta\hat{\mathbf{u}}^*\} \\ \{\Delta\mathbf{q}^{\mathbf{u}}\} \end{Bmatrix} = \begin{Bmatrix} \{\mathbf{b}^{\mathbf{u}}\} \\ \{\mathbf{b}_q^{\mathbf{u}}\} \end{Bmatrix} \quad (73)$$

where the components are given as:

$$\begin{aligned} [\mathbf{K}_{(k)}^{\mathbf{u}}] &= \int_{\Omega_0} \left[[\mathbf{G}_{(k)}^{\mathbf{u}}]^T : \mathbb{A}^t : [\mathbf{G}_{(k)}^{\mathbf{u}}] + \frac{\beta_{gu}}{\Delta t} [\hat{\mathbf{N}}_{(k)}^{\mathbf{u}}]^T [\hat{\mathbf{N}}_{(k)}^{\mathbf{u}}] \right] d\Omega_0 \\ [\mathbf{A}^{\mathbf{u}}] &= \int_{\Omega_0} \left[[\Theta^{\mathbf{u}}]^T : \mathbb{A}^t : [\Theta^{\mathbf{u}}] + \frac{\beta_{gu}}{\Delta t} [\phi^{\mathbf{u}}]^T [\phi^{\mathbf{u}}] \right] d\Omega_0 \\ [\mathbf{C}^{\mathbf{u}}] &= \int_{\Omega_0} \left[[\mathbf{G}_{(k)}^{\mathbf{u}}]^T : \mathbb{A}^t : [\Theta^{\mathbf{u}}] + \frac{\beta_{gu}}{\Delta t} [\hat{\mathbf{N}}_{(k)}^{\mathbf{u}}]^T [\phi^{\mathbf{u}}] \right] d\Omega_0 \\ \{\mathbf{b}^{\mathbf{u}}\} &= \int_{\Omega_0} [\hat{\mathbf{N}}_{(k)}^{\mathbf{u}}]^T \{\mathbf{T}^{t+\Delta t}\} d\Gamma_{0T} + \int_{\Omega_0} [\hat{\mathbf{N}}_{(k)}^{\mathbf{u}}]^T \{\mathbf{B}^{t+\Delta t}\} d\Omega_0 - \int_{\Omega_0} [\mathbf{G}_{(k)}^{\mathbf{u}}]^T \{\mathbf{P}\} d\Omega_0 \\ \{\mathbf{b}_q^{\mathbf{u}}\} &= \int_{\Omega_0} [\phi^{\mathbf{u}}]^T \{\mathbf{T}^{t+\Delta t}\} d\Gamma_{0T} + \int_{\Omega_0} [\phi^{\mathbf{u}}]^T \{\mathbf{B}^{t+\Delta t}\} d\Omega_0 - \int_{\Omega_0} [\Theta^{\mathbf{u}}]^T \{\mathbf{P}\} d\Omega_0 \end{aligned} \quad (74)$$

The size of the above matrices and vectors are:

$$\begin{aligned} \{\mathbf{b}^{\mathbf{u}}\} &: (3(m + m_{enr}(t + \Delta t)) \times 1) \\ [\mathbf{K}_{(k)}^{\mathbf{u}}] &: (3(m + m_{enr}(t + \Delta t)) \times 3(m + m_{enr}(t + \Delta t))) \\ [\mathbf{A}^{\mathbf{u}}] &: (3p \times 3p) \\ [\mathbf{C}^{\mathbf{u}}] &: (3p \times 3(m + m_{enr}(t + \Delta t))) \\ \{\mathbf{b}_q^{\mathbf{u}}\} &: (3p \times 1) \end{aligned}$$

Even for one scale of refinement, the number of potential hierarchical enrichment functions is larger than the existing hierarchical functions, i.e.

$$p > (m + m_{enr}(t + \Delta t)) \quad (75)$$

Instead of directly solving equations (73), static condensation is applied and the condensed form is written as:

$$\left([\mathbf{K}_{(k)}^{\mathbf{u}}] - [\mathbf{C}^{\mathbf{u}}]^T [\mathbf{A}^{\mathbf{u}}]^{-1} [\mathbf{C}^{\mathbf{u}}] \right) \{\Delta\hat{\mathbf{u}}^*\} = \{\mathbf{b}^{\mathbf{u}}\} - [\mathbf{C}^{\mathbf{u}}]^T [\mathbf{A}^{\mathbf{u}}]^{-1} \{\mathbf{b}_q^{\mathbf{u}}\} \quad (76)$$

For computational efficiency, the off-diagonal terms of $[\mathbf{A}^u]$ in Eq. (76) (that are relatively small) are neglected, and the approximate values of $\{\hat{\mathbf{u}}^*\}$ and $\{\mathbf{q}^u\}$ are solved from the equations:

$$\begin{aligned} \{\Delta \hat{\mathbf{u}}^*\} &\approx \left([\mathbf{K}_{(k)}^u] - [\mathbf{C}^u]^T [\mathbf{A}^u]^{-1} [\mathbf{C}^u] \right)^{-1} \left(\{\mathbf{b}^u\} - [\mathbf{C}^u]^T [\mathbf{A}_{ii}^u]^{-1} \{\mathbf{b}_q^u\} \right) \\ \{\Delta \mathbf{q}^u\} &\approx [\mathbf{A}_{ii}^u]^{-1} \left(\{\mathbf{b}_q^u\} - [\mathbf{C}^u] \{\Delta \hat{\mathbf{u}}^*\} \right) \end{aligned} \quad (77)$$

With the updated solution $\{\Delta \hat{\mathbf{u}}^*\}$ and $\{\Delta \mathbf{q}^u\}$ are obtained, a constitutive update based on these values is required to estimate the mechanical driving forces in Eq. (51i) for the crack propagation problem in the hierarchical space $V_{(k)}^{h(t+\Delta t)} = \text{span}\{N_1 \dots N_m, \varphi_1, \dots, \varphi_{m_{\text{enr}}(t+\Delta t)}, \phi_1, \dots, \phi_p\}$.

The phase field solution estimate \hat{s} can be subsequently obtained by solving a similar modified static condensation problem. The two components are given as:

$$\begin{aligned} \{\Delta \hat{s}^*\} &\approx \left([\mathbf{K}_{(k)}^s] - [\mathbf{C}^s]^T [\mathbf{A}^s]^{-1} [\mathbf{C}^s] \right)^{-1} \left(\{\mathbf{b}^s\} - [\mathbf{C}^s]^T [\mathbf{A}_{ii}^s]^{-1} \{\mathbf{b}_q^s\} \right) \\ \{\Delta \mathbf{q}^s\} &\approx [\mathbf{A}_{ii}^s]^{-1} \left(\{\mathbf{b}_q^s\} - [\mathbf{C}^s] \{\Delta \hat{s}^*\} \right) \end{aligned} \quad (78)$$

where

$$\begin{aligned} [\mathbf{K}_{(k)}^s] &= \int_{\Omega_0} \left[g_c l_c [\mathbf{G}_{(k)}^s]^T [\mathbf{G}_{(k)}^s] + \left(\frac{g_c}{l_c} + \hat{\mathbf{E}}^e : \mathbb{C}^e : \hat{\mathbf{E}}^e + \frac{\beta_{gs}}{\Delta t} \right) [\hat{\mathbf{N}}_{(k)}^s]^T [\hat{\mathbf{N}}_{(k)}^s] \right] d\Omega_0 \\ [\mathbf{A}^s] &= \int_{\Omega_0} \left[g_c l_c [\boldsymbol{\Theta}^s]^T [\boldsymbol{\Theta}^s] + \left(\frac{g_c}{l_c} + \hat{\mathbf{E}}^e : \mathbb{C}^e : \hat{\mathbf{E}}^e + \frac{\beta_{gs}}{\Delta t} \right) [\boldsymbol{\Phi}^s]^T [\boldsymbol{\Phi}^s] \right] d\Omega_0 \\ [\mathbf{C}^s] &= \int_{\Omega_0} \left[g_c l_c [\mathbf{G}_{(k)}^s]^T [\boldsymbol{\Theta}^s] + \left(\frac{g_c}{l_c} + \hat{\mathbf{E}}^e : \mathbb{C}^e : \hat{\mathbf{E}}^e + \frac{\beta_{gs}}{\Delta t} \right) [\hat{\mathbf{N}}_{(k)}^s]^T [\boldsymbol{\Phi}^s] \right] d\Omega_0 \\ \{\mathbf{b}^s\} &= \int_{\Omega_0} [\hat{\mathbf{N}}_{(k)}^s]^T \{\lambda_0^{t+\Delta t}\} d\Gamma_{0\lambda} + \int_{\Omega_0} [\hat{\mathbf{N}}_{(k)}^s]^T \left[-\mathbf{E}^e : \mathbb{C}^e : \hat{\mathbf{E}}^e + \hat{\psi}_d^t \right] d\Omega_0 \\ &\quad - \int_{\Omega_0} \left[g_c l_c [\mathbf{G}_{(k)}^s]^T [\mathbf{G}_{(k)}^s] + \left(\frac{g_c}{l_c} + \hat{\mathbf{E}}^e : \mathbb{C}^e : \hat{\mathbf{E}}^e \right) [\hat{\mathbf{N}}_{(k)}^s]^T [\hat{\mathbf{N}}_{(k)}^s] \right] d\Omega_0 \{s\}^t \\ \{\mathbf{b}_q^s\} &= \int_{\Omega_0} [\boldsymbol{\Phi}^s]^T \{\lambda_0^{t+\Delta t}\} d\Gamma_{0\lambda} + \int_{\Omega_0} [\boldsymbol{\Phi}^s]^T \left[-\mathbf{E}^e : \mathbb{C}^e : \hat{\mathbf{E}}^e + \hat{\psi}_d^t \right] d\Omega_0 \\ &\quad - \int_{\Omega_0} \left[g_c l_c [\boldsymbol{\Theta}^s]^T [\mathbf{G}_{(k)}^s] + \left(\frac{g_c}{l_c} + \hat{\mathbf{E}}^e : \mathbb{C}^e : \hat{\mathbf{E}}^e \right) [\boldsymbol{\Phi}^s]^T [\hat{\mathbf{N}}_{(k)}^s] \right] d\Omega_0 \{s\}^t \end{aligned} \quad (79)$$

where $\hat{\psi}_d = \frac{1}{2} \sum_{\alpha, \beta}^N h^{\alpha\beta} |\gamma^\alpha| |\gamma^\beta|$. Eq. (77) and (78) identify the solution estimate $\hat{\mathbf{u}}$ and \hat{s} for the $k+1$ -th iteration of hierarchical enhancement algorithm in Section 4.2.1.

5. Wavelets as optimal enrichment basis functions

The second generation wavelet functions [63] have been shown to provide an optimal basis of hierarchical enrichment functions for linear elastic problems in [61] and nonlinear crystal plasticity problems in [62]. This section explores the adoption of lifted second generation wavelets as basis functions for optimal hierarchical enrichment that conform to the profile of the phase field solution estimate \hat{s} in Eq. (67). The procedure of generating wavelets-based enrichment basis for displacement estimate $\hat{\mathbf{u}}$ is provided in detail in [62] and will not be elaborated here.

The following properties of wavelet functions render wavelets ideal for multi-resolution hierarchical enrichment.

- **Compact support:** Wavelet functions have compact support on each subdomain of Ω . Solutions interpolated on wavelet function bases do not exhibit spurious instabilities such as the Gibbs phenomena.
- **Multi-resolution:** Wavelet bases have multi-resolution characteristics, which resolve the difference between hierarchical scales. This implies that wavelet basis functions associated with negligible coefficients indicate that higher scale enrichment is not necessary.

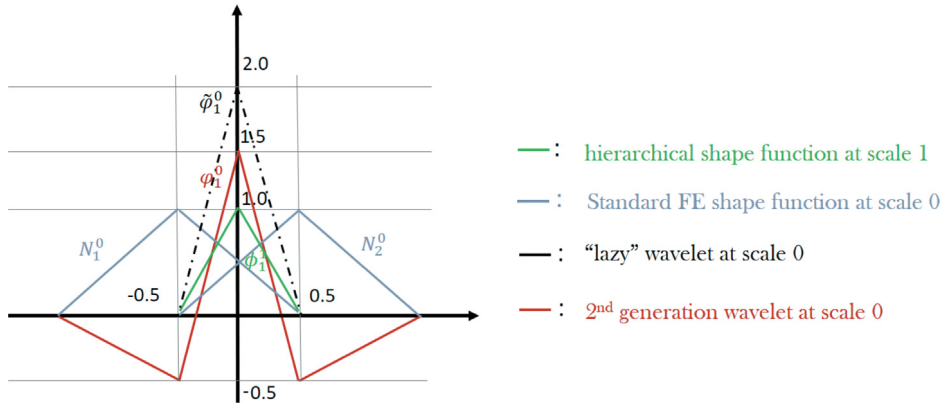


Fig. 4. Generating wavelet bases with the lifting scheme in a 1D hierarchical finite element mesh.

- *Compatibility with FE discretization:* Second-generation wavelets functions [63,65] may be constructed from any irregular hierarchical finite element mesh. Errors due to nonconformity are consequently avoided in the wavelet-enriched discretization spaces.

As detailed in [61], the following criteria are adopted to generate the wavelet enrichment functions

- *Riesz basis:* Wavelet functions with the Riesz basis property avoid aliasing by ensuring completeness of each scale of wavelet functions.
- *Vanishing moments:* The integral of wavelet functions over any domain is zero, so that a small coefficient has negligible contribution.
- *Hierarchical characteristics:* The wavelet family is constructed from the coarse FEM mesh.

Lifted second generation wavelets e.g. in [63,65] naturally conform to these criteria.

The procedure to create a wavelet from hierarchical finite element shape function employs a lifting scheme [61,63]. First, a “lazy” wavelet is created from a hierarchical shape functions as:

$$\tilde{\varphi}_\beta^{l-1}(\mathbf{X}) = \bar{\alpha} \phi_\beta^l(\mathbf{X}) \quad (80)$$

where $\bar{\alpha}$ is a constant and l denotes the hierarchical scale. Second, this wavelet is transformed through the lifting scheme, in which vanishing moments are added. Each scale of wavelets becomes a Riesz basis of the domain Ω_0 , expressed as:

$$\varphi_\beta^{l-1}(\mathbf{X}) = \tilde{\varphi}_\beta^{l-1}(\mathbf{X}) - \sum_{\lambda}^R a_\lambda N_\lambda^{l-1}(\mathbf{X}) \quad (81)$$

where the function N_λ^{l-1} is a standard finite element shape function at scale $l-1$. The coefficient a_λ is chosen such that:

$$\int_{\Omega} \varphi_\beta^{l-1}(\mathbf{X}) d\Omega = 0 \quad \forall \beta \in [1, p(l)] \quad (82)$$

Adding the functions N_λ^{l-1} extends the compact support of the wavelet function φ_β^{l-1} to the whole domain, i.e.

$$\bigcup_{\beta}^{p(l)} \text{supp}(\varphi_\beta^{l-1}) = \Omega_0 \quad (83)$$

The lifting scheme with $R = 2$ is sufficient to satisfy all the properties mentioned above. The lifting scheme for a 1D domain is shown in Fig. 4 with $R = 2$, $\bar{\alpha} = 2$ and $a_\lambda = 0.5$. The support of φ_1^0 extends to $x \in [-1.5, 1.5]$, while $\tilde{\varphi}_1^0$ is non-zero for $x \in [-0.5, 0.5]$. Furthermore, $\int_{-1.5}^{1.5} \varphi_1^0(X) dX = 0$. The estimate $\tilde{s}(\mathbf{X})$ is projected on a

wavelet basis of l scales, constructed upon the coarse finite element discretization space, as:

$$\tilde{s}^l(\mathbf{X}) = \sum_{\alpha}^m c_{\alpha}^s N_{\alpha}(\mathbf{X}) + \sum_j^l \sum_{\beta}^{p(j)} d_{\beta}^{s,j-1} \phi_{\beta}^{j-1}(\mathbf{X}) \quad (84)$$

where $\{\phi^j\}^{p(j)}$ is a family of $p(j)$ wavelet function at scale j . The coefficients c^s and $d^{s,j}$ are obtained by a fast wavelet transform method discussed in [61,65]. Using the multi-resolution property, wavelet bases with small coefficients may be omitted with negligible interpolation error. This leads to the criterion for selecting enrichment functions, expressed as:

$$\{\phi\}^{m_{enr},s} = \{\phi_{\gamma}^{j-1} \mid d_{\gamma}^{s,j-1} > \bar{\epsilon}^s, \gamma = 1, \dots, p(j), j = 1, \dots, l\} \quad (85)$$

where $\bar{\epsilon}^s$ is the tolerance for the phase field parameter in Eq. (84). The projection $P(\tilde{s}^l)(\mathbf{X})$ of the phase field estimates $\tilde{s}(\mathbf{X})$ on the enrichment basis $\{\phi\}^{m_{enr},s}$, and is written as:

$$P(\tilde{s}^l)(\mathbf{X}) = \sum_{\alpha}^m c_{\alpha}^s N_{\alpha}(\mathbf{X}) + \sum_j^l \sum_{\gamma \mid \{d_{\gamma}^{s,j-1} > \bar{\epsilon}^s\}}^{p(j)} d_{\gamma}^{j-1} \phi_{\gamma}^{j-1}(\mathbf{X}) \quad (86)$$

Combining equation (84) with Eq. (87) yields:

$$\tilde{s}^l(\mathbf{X}) - P(\tilde{s}^l)(\mathbf{X}) \leq \sum_j^l \sum_{\gamma \mid \{d_{\gamma}^{s,j-1} \leq \bar{\epsilon}^s\}}^{p(j)} \bar{\epsilon}^s \phi_{\gamma}^{j-1}(\mathbf{X}) \quad (87)$$

This leads to the following desired property of the projection error:

$$\|\tilde{s}^l(\mathbf{X}) - P(\tilde{s}^l)(\mathbf{X})\|^2 \leq C_2 |\bar{\epsilon}^s|^2 \quad (88)$$

An upper bound for C_2 may be given as $C_2 \leq \sum_j^l C^j \hat{p}(j)$, where $\hat{p}(j)$ is the number of wavelet bases that are omitted at scale j and C^j is the Riesz upper bound of the wavelet basis at scale j . Since the wavelets are constructed from hierarchical shape functions, Eq. (87) is rewritten as:

$$P(\tilde{s})(\mathbf{X}) = \sum_{\alpha}^m e_{\alpha} N_{\alpha}(\mathbf{X}) + \sum_j^l \sum_{\gamma}^{m_{enr,s}(j)} f_{\gamma}^j \phi_{\gamma}^j(\mathbf{X}) \quad (89)$$

with e_{α} and f_{β}^j expressed as functions of c^s and d^s . These coefficients are not important for the method, and only the set of enrichment functions is sought. Eq. (89) provides a set of $m_{enr} = \sum_j^l m_{enr}(j)$ enrichment functions $\phi_{\beta}^j(\mathbf{X})$. This set is used as the next scale of enrichment functions for the phase field problem, such that:

$$\{\phi\}^{m_{enr},s} = \bigcup_j^l \{\phi^j\}^{m_{enr,s}(j)} \quad (90)$$

Similarly, as described in [61], the selection of enrichment functions for the displacement field is expressed as:

$$\{\phi\}^{m_{enr},u} = \{\phi_{\gamma}^{j-1} \mid d_{\gamma}^{u,j-1} > \bar{\epsilon}^u, \gamma = 1, \dots, p(j), j = 1, \dots, l\} = \bigcup_j^l \{\phi^j\}^{m_{enr,u}(j)} \quad (91)$$

5.1. Projection of internal variables on the new mesh

An important consideration with adaptive methods for nonlinear history dependent problems is the projection of internal variables from the old mesh to the new mesh. These variables include the mechanical stiffness and internal variables $\mathcal{I}^{mech} = \{\mathbb{A}, \mathbf{P}, \mathbf{F}^p, g^{\alpha}, \gamma^{\alpha}\}$ at time t in the mechanical problem in Eq. (74), as well as the phase field internal variables $\mathcal{I}^{pf} = \{\hat{\mathbf{E}}^e : \mathbb{C}^e : \hat{\mathbf{E}}^e, \mathbf{E}^e : \mathbb{C}^e : \hat{\mathbf{E}}^e, \hat{\psi}_d\}$ in phase field problem in Eq. (79). They are not known *a-priori* for the added enrichment functions and must be projected from the known values in the discretization space of the previous increment. This is at a coarser resolution than the one for which $\tilde{\mathbf{u}}$ and \tilde{s} will be estimated. For a

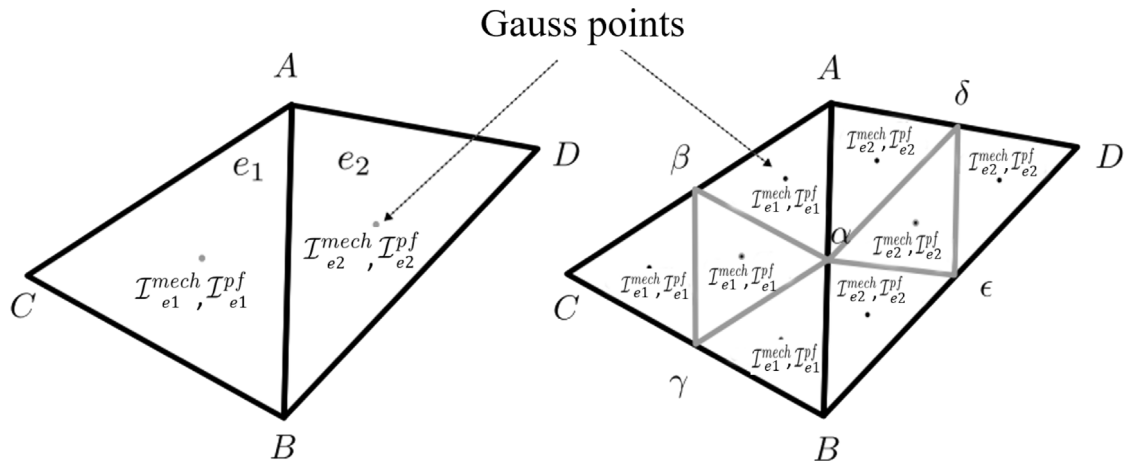


Fig. 5. Projecting stress and tangent stiffnesses to adapted subdivided (child) elements from parent elements.

discretized space, represented in part by linear interpolation functions, the internal variables are calculated at Gauss point and constant in each element and discontinuous at the element boundaries Γ_e . Hence they are known for all x in $\Omega|\Gamma_e$. The internal variables in the new discretization space are directly projected from their respective values in the old discretization space at relevant Gauss points, as shown with a two dimension example in Fig. 5. This uniform projection approach enforces the conservation of the internal variables based on the previous equilibrium conditions since the finer elements constitute a complete subdivision of their parent element. It does not take any ad-hoc correction and is therefore a conservative choice. Higher order interpolation methods can be used to obtain the internal variables associated with new elements, which may lead to higher convergence rate of the non-linear algorithm.

6. Numerical simulations with the adaptive CP-PF FE model

The basic phase field formulation with crystal elasticity model for polycrystalline microstructures has been validated in a recent paper in [51]. This section focuses on examining the effectiveness of the wavelet-enriched adaptive coupled crystal plasticity-phase field finite element model (CP-PF FEM) in simulating crack propagation in polycrystalline microstructures. In the first example, the accuracy and efficiency of the proposed wavelet enhancements are evaluated for crack propagation in Section 6.1. The computational model of a 41-grain polycrystalline microstructure of a titanium alloy Ti-6V-4Al is developed and simulated. The microstructure of this alloy consists of alternating laths of two phases, viz. an α phase with a *hcp* crystalline structure and a β phase with a *bcc* crystalline structure. In [68,79] a homogenized model incorporating the individual volume fractions of the α and β lath structure in the colonies is developed following the rule of mixtures. The equivalent model takes into account the deformation produced by multiple slip systems in the α and β phases. This constitutive model is adopted for the Ti-6V-4Al alloy. In the next example of Section 6.2, a larger polycrystalline microstructural RVE of the Ti-6V-4Al alloy containing 513 grains is simulated to study the interaction between crack propagation and local microstructure. Macroscopic stress-strain response are also compared in this example.

Constitutive parameters in the crystal plasticity model in Section 2.6 are calibrated from results of uni-axial tension and fatigue tests of the Ti-6V-4Al alloy provided in [80]. The calibration process follows methods discussed in [81]. Phase field parameters are assumed for this analysis. The calibrated elasticity, crystal plasticity and phase field parameters are listed in Table 1.

6.1. Convergence study with the wavelet-enriched hierarchical FE model for the phase field crack model

The computational model of a 41-grain polycrystalline Ti-6V-4Al microstructure is shown in Fig. 6. The accuracy and efficiency of the wavelet-enriched adaptive coupled CP-PF FE model is evaluated in this section. The computational model needs crystallographic lattice orientation data for individual grains in the polycrystalline

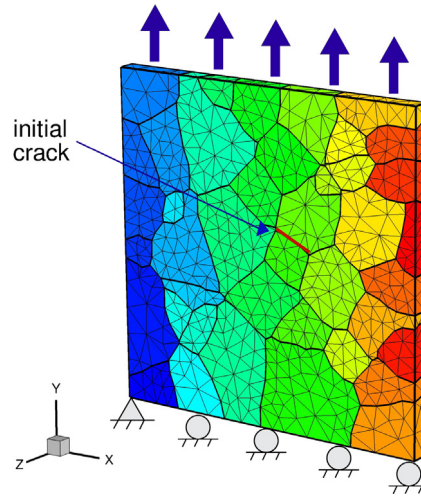


Fig. 6. Computational model of a 41-grain polycrystalline microstructure of a titanium alloy Ti-6V-4Al showing boundary and loading conditions. A small initial crack is embedded along a grain boundary inside the microstructure in the form of predefined $s = 1$.

Table 1

Crystal plasticity constitutive parameters for the *hcp* and *bcc* slip systems in the Ti-6V-4Al alloy.

C_{11}	C_{12}	C_{13}	C_{33}	C_{44}	G_c (phase field)
170 GPa	98 GPa	86 GPa	204 GPa	51 GPa	$200 Jm^{-2}$
m	$\dot{\gamma}_0$	r	n	$h_s(BCC)$	τ_s (BCC)
0.02	$0.001 s^{-1}$	0.1	0.01	25	200 MPa
$(g_0^\alpha)_{bas}$	$(g_0^\alpha)_{pri}$	$(g_0^\alpha)_{pyr(a)}$	$(g_0^\alpha)_{pyr(c+a)}$	$(g_0^\alpha)_{bcc(c+a)}$	
354 MPa	354 MPa	425 MPa	505 MPa	200 MPa	
$(g_s^\alpha)_{bas}$	$(g_s^\alpha)_{pri}$	$(g_s^\alpha)_{pyr(a)}$	$(g_s^\alpha)_{pyr(c+a)}$	$(h_0^\beta)_{hcp}$	$(h_0^\beta)_{bcc}$
470 MPa	570 MPa	570 MPa	1550 MPa	300 MPa	1500 MPa
$(q)_{bas-all}$	$(q)_{pri-all}$	$(q)_{pyr-all}$	$(q)_{bcc-bcc}$	K_{hcp}^α	$K_{soft/hard,bcc}^\alpha$
1.0	1.0	1.0	1.0	164.5	413.4 / 315.9

ensemble. This is obtained from electron back scatter diffraction (EBSD) image data of the Ti-6V-4Al alloy in [80]. The data is input into the 3D microstructure reconstruction software DREAM.3D [82] for constructing the microstructural domain shown in Fig. 6. The computational domain contains 41 grains and has a dimension of $80 \mu m \times 80 \mu m \times 4 \mu m$. The average equivalent grain diameter on XY plane is $\sim 12 \mu m$. Prior to adaptive enrichment, it is discretized into an initial coarse-scale mesh of 5410 TET4 elements with 1554 nodes. The 41-grain ensemble is statistically insufficient to represent the macroscopic material characteristics. It is created only to test the effectiveness of the wavelet enriched adaptive algorithm.

The wavelet-enriched adaptive coupled FE model is used to simulate brittle and ductile crack propagation, respectively using crystal elasticity and crystal plasticity constitutive relations. The crystal elasticity model considers the elastic properties of the single crystals with the plastic flow suppressed, i.e. by enforcing $\dot{\gamma}_\alpha = 0 \forall \alpha \in [1, \dots, n_{slip}]$ in Eqs. (51e). The crystal plasticity constitutive model is described by Eqs. (51c)–(51g). A reference solution for each case is created by running the coupled FE model, described in Section 3.1, on a highly refined mesh containing 346240 TET4 elements and 67045 nodes, but without any adaptive enrichment.

6.1.1. Brittle crack problem

The brittle crack propagation test is considered first. An initial crack is placed inside the microstructure along a short grain boundary by setting $s = 1$ on the grain boundary nodes, as shown in Fig. 6. The microstructure is subjected to a uniaxial tensile strain along Y-axis by applying a constant strain-rate $\dot{\epsilon} = 1 \times 10^{-3}$ displacement boundary condition on $Y = 80 \mu m$ surface and fixing u_Y on the $Y = 0$ surface. All rigid body degrees of freedom are

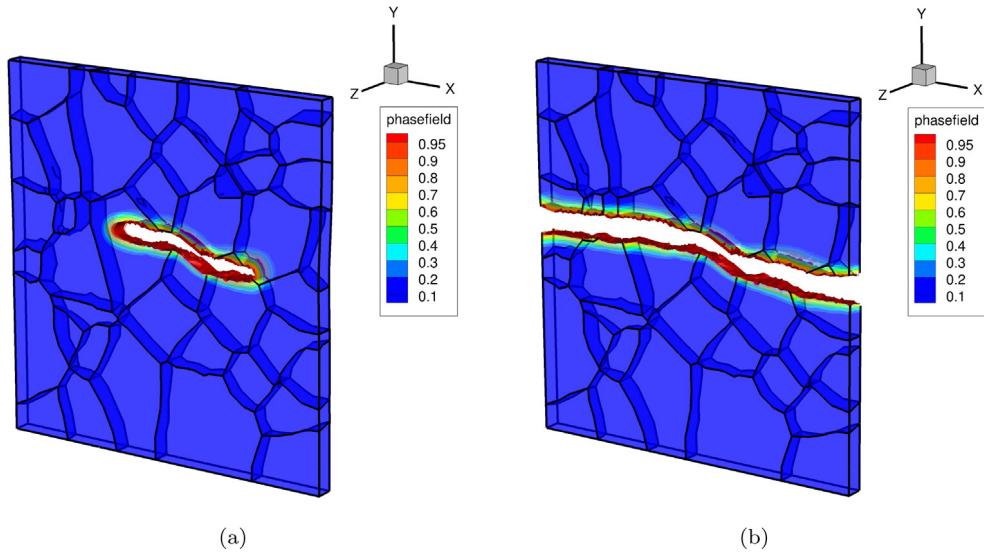


Fig. 7. Contour plots of the phase field order parameter s in the deformed configuration from brittle crack propagation simulations using a crystal elasticity model for: (a) 1.4% volume-averaged true strain and (b) 1.6% volume-averaged true strain.

suppressed for the computational model. A crack characteristic length scale parameter $l_c = 1 \mu\text{m}$ and critical fracture energy density $G_c = 30 \text{Jm}^{-2}$ are used in these simulations. Adaptive enrichment for this example is capped at two scales of hierarchical enrichment functions $\{\phi\}^n$, as defined in Section 4.2.1. This is considered to be sufficiently fine for the given l_c . The adaptive enrichment is triggered with a displacement tolerance of $\bar{\epsilon}^u = 0.01$ and phase field tolerance of $\bar{\epsilon}^s = 0.01$. Figs. 7(a) and 7(b) depict contour plots of the phase field variable s and the corresponding crack propagation for 1.4% and 1.6% applied strains, respectively. The corresponding nodal positions of enrichment functions $\{\varphi\}^{m_{enr}}$ in the 2-scale wavelet-basis enriched hierarchical adaptive grid are plotted in Figs. 8(a) and 8(b) on the undeformed configuration. The enrichment nodes are located along the path of crack propagation, where the coarse scale element interpolation error is large. In this case it is observed that the nodal enrichment is triggered primarily by the phase field error in Eq. (88), and the displacement error on wavelet projection is much smaller.

Fig. 9(a) shows the convergence rate in terms of the phase field error, calculated as the percentage error of the L_2 norm of solution field. It is expressed as:

$$e^s = \frac{\|s^{h_{enr}}(\mathbf{X}) - s^f(\mathbf{X})\|^2}{\|s^f(\mathbf{X})\|^2} \times 100 (\%) \quad (92)$$

where s^f is the reference phase field solution. Simulation results using a hierarchical h -adapted FEM is also provided in Fig. 9 for comparison. Here the h -adaptation hierarchically refines TET4 elements when the phase field parameter reaches a threshold value. Specifically a n -scale TET4 element is uniformly subdivided into 8 $(n+1)$ -scale TET4 elements when the phase field parameter value at its integration point satisfies $s > n * 0.25$. This adaptivity is known to provide at least the same or better convergence-rate as classical h -adaptivity [59,60]. The wavelet-enriched adaptive coupled FE model consistently converges faster ($\mathcal{O}(\mathcal{N}^{-3.797})$) than the hierarchical h -adapted FEM model ($\mathcal{O}(\mathcal{N}^{-1.385})$). This convergence-rate for the phase field error is significantly higher than that for the displacement error. This is because the phase field crack propagation is highly sensitive to the mesh resolution, as demonstrated in Section 4.1. Fig. 8(c) shows the location of the enrichment nodes for the hierarchical h -adapted FEM at 1.6% strain. The comparison between Figs. 8(b) and 8(c) clearly shows the significant advantage of the wavelet adapted method over the h -adapted method. The former requires much less enrichment nodes for crack propagation for comparable accuracy, as also seen in Fig. 9(a). The number of enrichment nodes as a function of crack length by the two methods is compared in Fig. 9(b). After the crack has propagated through the microstructure at 1.6% volume-averaged true strain, the total number of nodes for the wavelet adapted FEM is 2790, as opposed to 10244 nodes with the h -adapted FEM. The using of wavelets to provide optimal enrichment basis

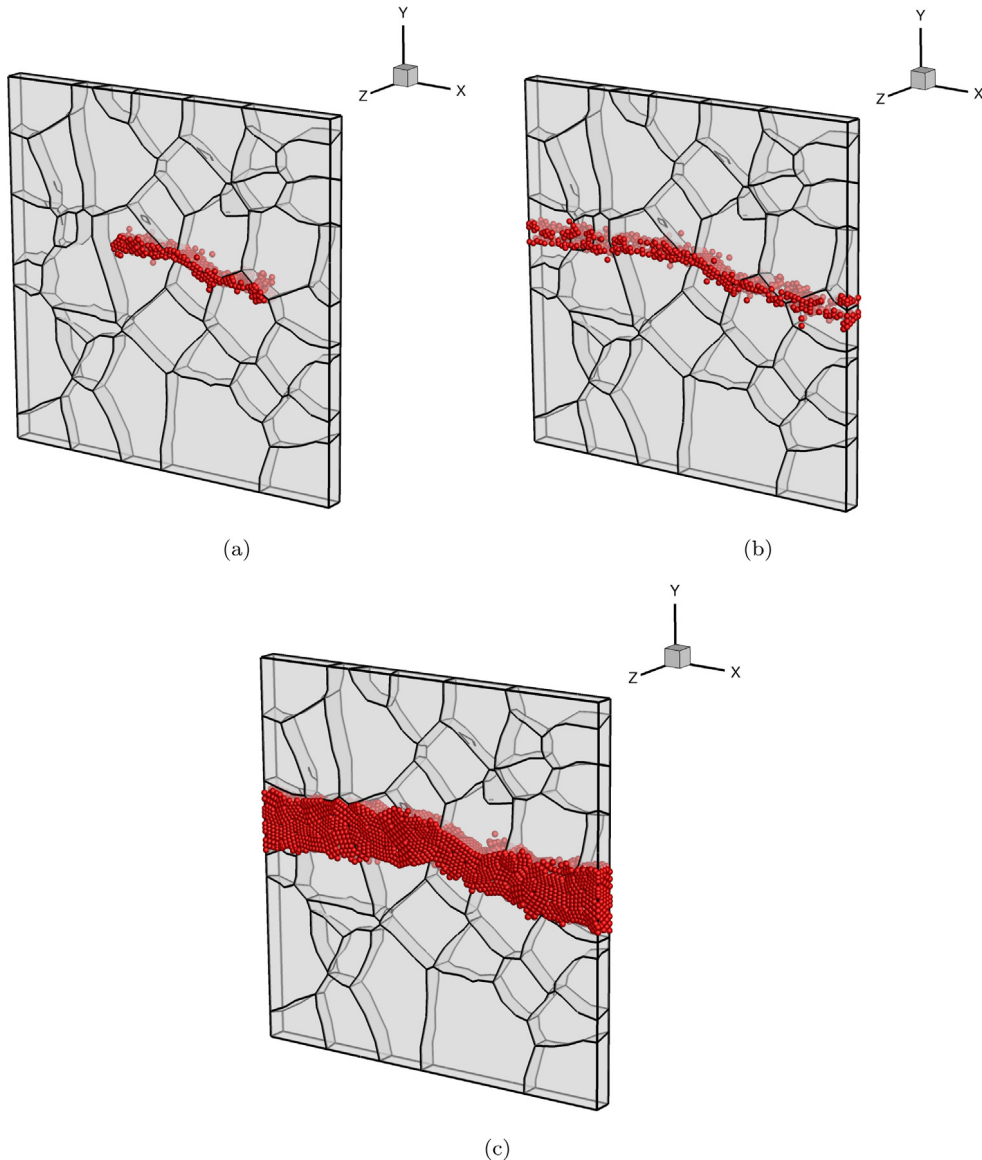


Fig. 8. Location of nodes associated with adaptive hierarchical FEM (shown in the undeformed configuration): (a) with second generation wavelet enrichment at 1.4% volume-averaged true strain, (b) with second generation wavelet enrichment at 1.6% volume-averaged true strain, and (c) hierarchical h-adapted FEM at 1.6% volume-averaged true strain.

1 functions reduces the number of required enrichment nodes significantly for high accuracy in the crack propagation
 2 problem.

3 6.1.2. Ductile crack problem

4 Next, the ductile crack propagation behavior by the wavelet-enriched hierarchical FE model is studied by
 5 activating the full crystal plasticity model. The same applied boundary conditions are applied as in Section 6.1.1.
 6 Also the same adaptive enrichment tolerance $\bar{\epsilon}^u = 0.01$ and $\bar{\epsilon}^s = 0.01$ are used for the simulations. The length
 7 scale parameter is $l_c = 2 \mu\text{m}$ and critical fracture energy density $Gc = 700 \text{ J m}^{-2}$. Contour plots of the simulated
 8 crack phase field parameter s at 7.6% and 13.0% applied strain are shown in Figs. 10(a) and 10(b) respectively.
 9 Due to the energy dissipation due to plastic flow, additional deformation is required to propagate the crack tip.

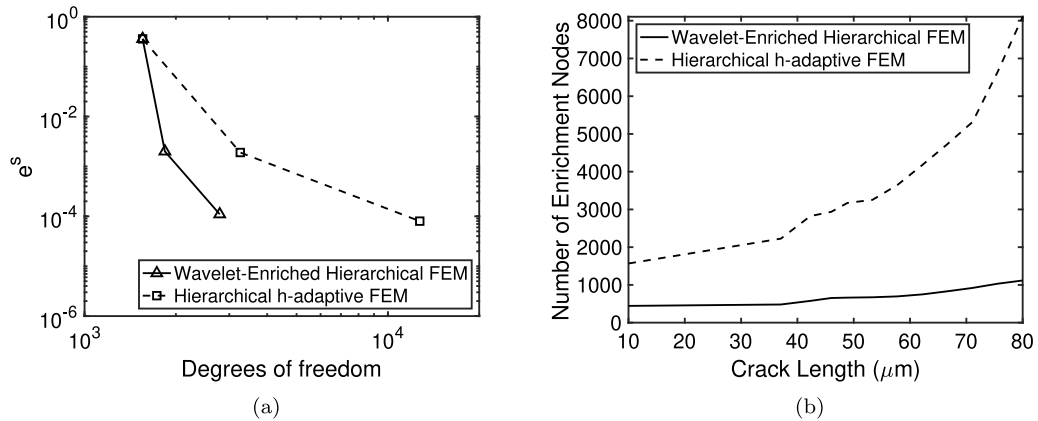


Fig. 9. (a) Convergence rates (on a log—log plot) of the error e^s in Eq. (92) as a function of the degrees of freedom, and (b) the number of enrichment nodes as a function of the crack length, for simulations of brittle crack propagation by the wavelet adapted and h-adapted FEM.

The crack, in this case, is thicker with a blunt crack tip compared to the brittle crack in Section 6.1.1. The crack path is also different from the brittle crack as seen from Figs. 7(b) and 10(b). For the brittle crack, the crack path is almost straight and shows less effects of crystallographic orientation of the grains in the ensemble. For ductile crack propagation, the crack path is found to depend on the crystallographic orientation as it moves through each grain. The Von Mises stress field during brittle and ductile cracking through half of the microstructure is compared in Figs. 12(a) and 12(b). Stress concentration ahead of the brittle crack tip is much higher than that for the ductile crack. The gradient of stress is also higher for brittle crack propagation, while the dislocation slips during ductile crack propagation diffuse the stress field. It is also observed the crack propagation velocities at the two crack tips for ductile cracking are different. In Fig. 12(b), the crack in the $X+$ direction has already propagated through the microstructure, while the other tip in the $X-$ direction has not propagated as much. This is a consequence of the grain orientations. *Hard grains*, for which slip systems are oriented to inhibit plastic flow due to high slip system resistance will induce high stress concentration and thereby facilitate crack propagation. *Soft grains* on the other hand are ideally oriented for high dislocation glide and plastic flow. These grains dissipate considerable plastic energy that will hinder crack propagation and render the crack tip blunt.

The location of second generation wavelet nodes, corresponding to hierarchical enrichment in ductile crack propagation, at 7.6% and 13.0% volume-averaged true strains are plotted in Figs. 11(a) and 11(b) respectively (in the undeformed configuration). The convergence rate with respect to the phase field error is shown in Fig. 13(a). The average convergence rate for the wavelet-enriched FEM is ($\mathcal{O}(\mathcal{N}^{-6.968})$) compared to ($\mathcal{O}(\mathcal{N}^{-2.325})$) for the h-adapted FEM. At 7.6% volume-averaged true strain, the total number of nodes in the wavelet-enriched FEM simulation is 3046, whereas it requires 15750 nodes to solve the same problem with the h-adapted FEM. The number of fine-scale enrichment nodes is plotted as a function of the evolving crack length for the two methods in Fig. 13(b). Once again, there is a large difference in the number of enrichment nodes with crack propagation. The wavelet-adapted FEM is far superior than the h-adapted FEM in terms of the added nodes for similar accuracy in ductile crack propagation. These examples demonstrate the high potential of the wavelet-enriched adaptive hierarchical FEM for solving the coupled mechanical-crack phase field problem for simulating crack propagation in polycrystalline microstructures.

6.2. Simulating ductile crack propagation in a polycrystalline microstructural SERVE

The statistically equivalent RVE or *SERVE* [83,84] is an optimal microstructural domain, for which statistical distribution functions of morphological parameters, as well as material properties converge to those for the experimental microstructure in electron back-scatter diffraction (EBSD) or scanning electron microscopy (SEM) images. A polycrystalline *SERVE* of the Ti-6V-4Al alloy is created using the DREAM.3D software [82] from EBSD data in [80]. The polycrystalline microstructural *SERVE*, shown in Fig. 14(a), has dimensions $80 \mu\text{m} \times 80 \mu\text{m} \times 80 \mu\text{m}$

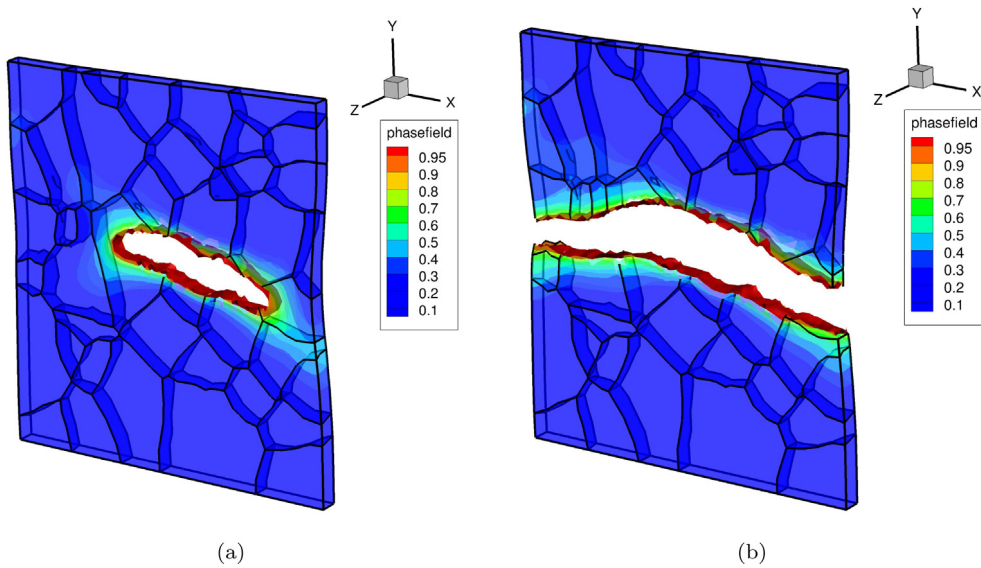


Fig. 10. Contour plots of the phase field order parameter s in the deformed configuration from ductile crack propagation simulations using a crystal plasticity model for: (a) 7.6% volume-averaged true strain and (b) 13.0% volume-averaged true strain.

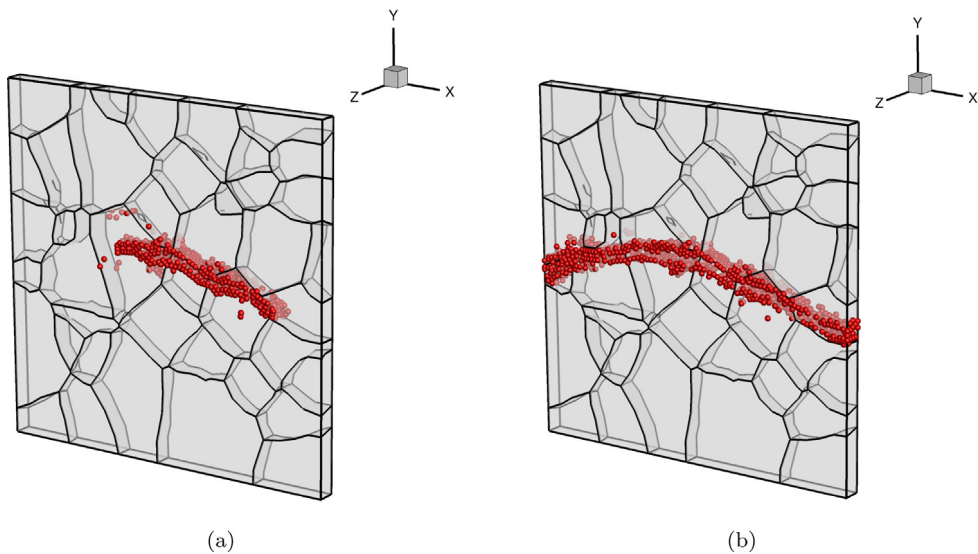


Fig. 11. Location of nodes associated with adaptive hierarchical FEM (shown in the undeformed configuration) with second generation wavelet enrichment for ductile fracture at: (a) 7.6% volume-averaged true strain, and (b) 13.0% volume-averaged true strain.

1 and consists of 513 grains. Simulations are conducted with the adaptive, wavelet-enriched hierarchical CP-PF FE
 2 model to evaluate its effectiveness in predicting ductile crack propagation in polycrystalline microstructures. The
 3 initial mesh consists of 67601 TET4 elements with 12305 nodes. The constitutive model parameters are tabulated
 4 in Table 1 and the characteristic length scale parameter is $l_c = 2 \mu\text{m}$. Constant strain-rate displacement boundary
 5 conditions are applied on the top surface ($X = 80 \mu\text{m}$) and the bottom surface ($X = 0$) is fixed in the X direction.
 6 All rigid body motions are suppressed. Two hierarchical scales are used for the adaptive wavelet enrichment in the

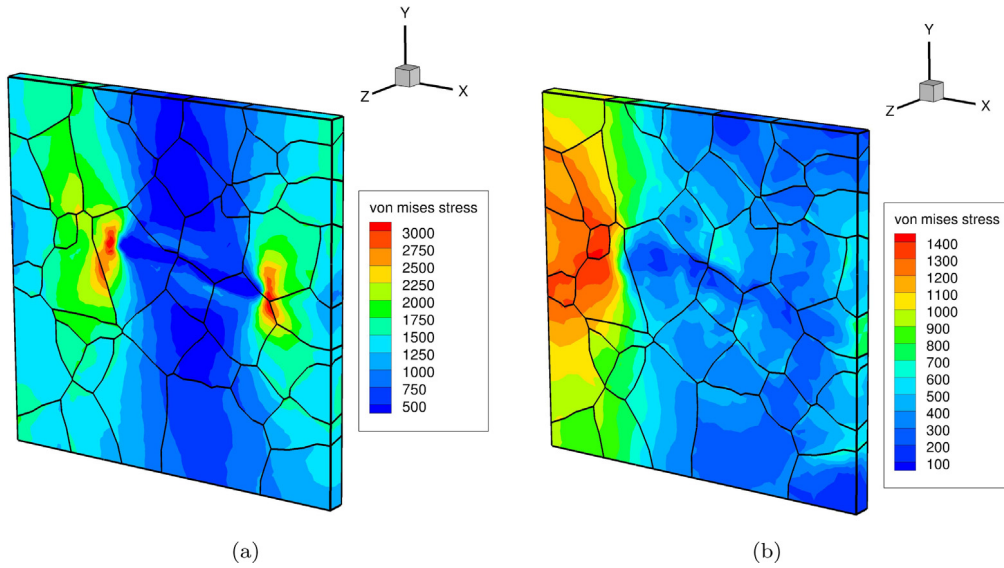


Fig. 12. Von Mises stress distribution for (a) brittle crack propagation at 1.4% volume-averaged true strain, and (b) ductile crack propagation at 8.5% volume-averaged true strain, both plotted in the deformed configuration.

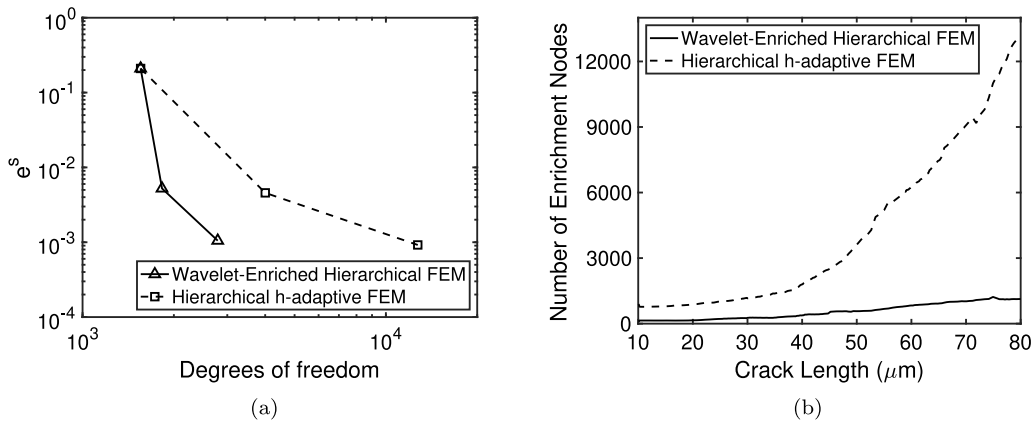


Fig. 13. (a) Convergence rates (on a log-log plot) of the error e^s in Eq. (92) as a function of degrees of freedom, and (b) comparison of number of enrichment nodes, for simulation of ductile crack propagation by the wavelet-adapted and h-adapted FEM using crystal plasticity model.

FEM simulation. The adaptive enrichment is triggered with a displacement tolerance of $\bar{\epsilon}^u = 0.01$ and phase field tolerance of $\bar{\epsilon}^s = 0.01$. An initial crack nucleus is placed on a *hard-soft* grain boundary inside the microstructure by pre-defining the nodal order parameter as $s = 1$. This is shown in Fig. 14(b). This grain boundary is characterized by a near 90° c -axis misorientation between contiguous grains, where the soft grain is favorably oriented for time-dependent plastic flow, while the hard grain impedes plastic flow [45,46]. The crack at this nucleus starts to propagate until after 5.5% volume-averaged true strain, when the local driving energy, consisting of the terms $\rho_0 \frac{\partial \psi^e}{\partial s}$ and $\rho_0 \frac{\partial \psi^d}{\partial s}$ in Eq. (61), become sufficiently high.

Fig. 15(a) shows the contour plots of the phase field parameter when the crack starts to propagate at 5.7% volume-averaged true strain. At 6.4% true strain, the crack has propagated through the entire microstructure, as shown in Fig. 15(b). Fig. 16(b) shows the Von-Mises stress distribution at 5.7% volume-averaged true strain. The volume-averaged stress-strain response of the polycrystalline SERVE is plotted in Fig. 16(b). As the crack propagates, it degrades the material's stress-carrying capacity as well as the elastic and defect energy, causing a drop in the stress. As shown in Fig. 15(b), the crack does not propagate in a straight path, but takes a sharp turn downward near the

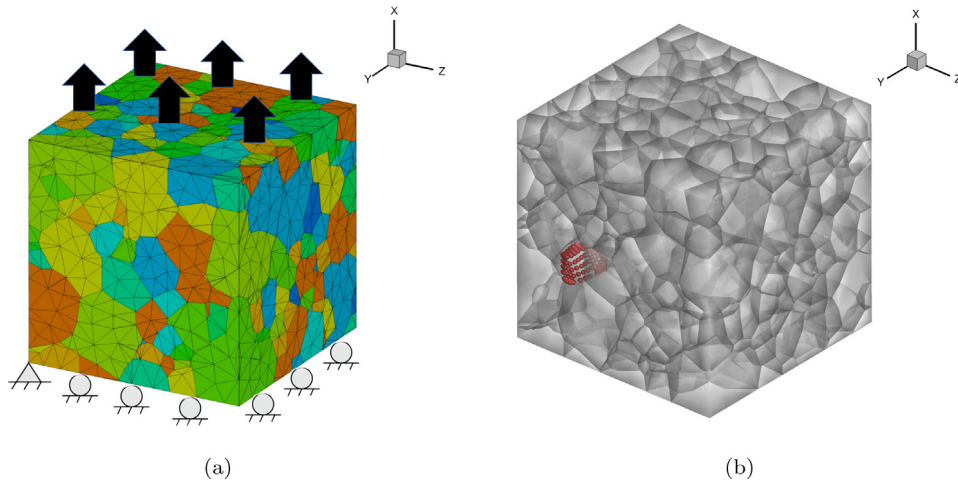


Fig. 14. (a) Illustration of the computational model of a polycrystalline microstructural SERVE containing 512 grains of the titanium alloy Ti-6V-4Al showing boundary and loading conditions, and (b) nodes depicting the location of initially embedded crack nucleus with predefined $s = 1$.

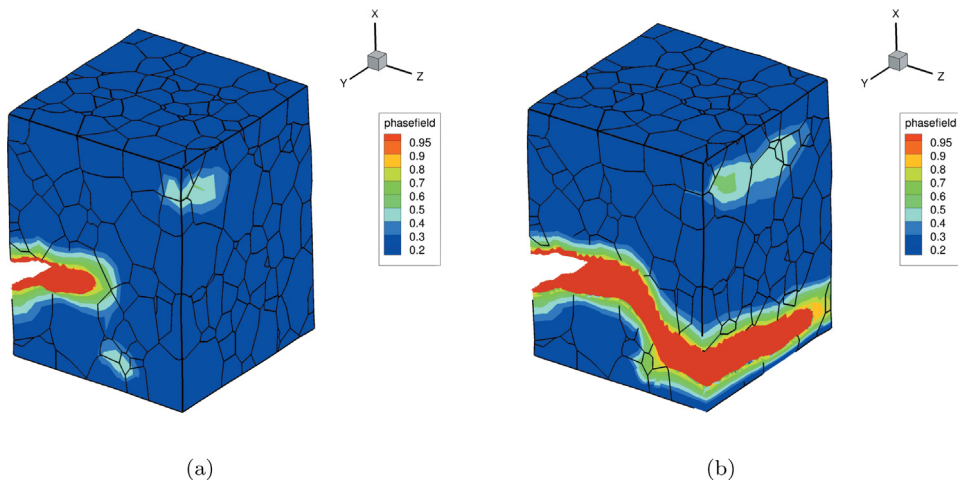


Fig. 15. Contour plots of the phase field order parameter s in the deformed configuration from ductile crack propagation simulations of the 513 grains microstructural SERVE at: (a) 5.7% volume-averaged true strain and (b) 6.4% volume-averaged true strain.

middle of the microstructure. The direction is affected by the hard grains traversed by the crack, causing higher stress concentration as indicated in Fig. 16(a). The figure shows an unsymmetric distribution of the stress in grains ahead of the crack tip. The higher stress field in the lower grains causes the crack to veer downwards.

Figs. 17(a) and 17(b) show the lifted second generation wavelet-based multi-resolution nodal enrichment (in the undeformed configuration) at 5.7% and 6.4% strains respectively. The enrichment nodes are generally located along the crack path. Additionally, a few regions away from the propagating crack path, which have phase field concentration and are potential locations of new crack nucleation, also have enrichment nodes. The evolution of fine scale nodes, associated with wavelet enrichment functions, is plotted as a function of the evolving crack surface area in Fig. 18. At 6.4% strain, a total number of 24727 nodes are activated in the simulation with wavelet-enriched hierarchical adaptive FEM. In comparison, approximately 130000 nodes are needed if the simulation is run on the same scale of fine mesh with the hierarchical h-adapted FEM. Again, this example demonstrates the robustness and efficiency advantages of the wavelet-enriched adaptive hierarchical FEM for simulating crack propagation in polycrystalline microstructures.

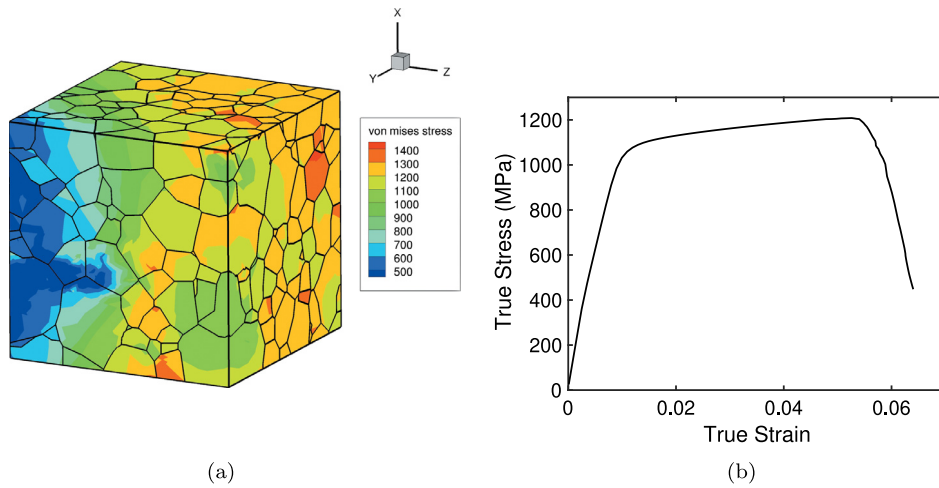


Fig. 16. (a) Von-Mises stress distribution during crack propagation at 5.7% volume-averaged true strain (plotted in the undeformed configuration), and (b) the volume-averaged stress–strain response of the polycrystalline SERVE using the coupled CP-PF FE model.

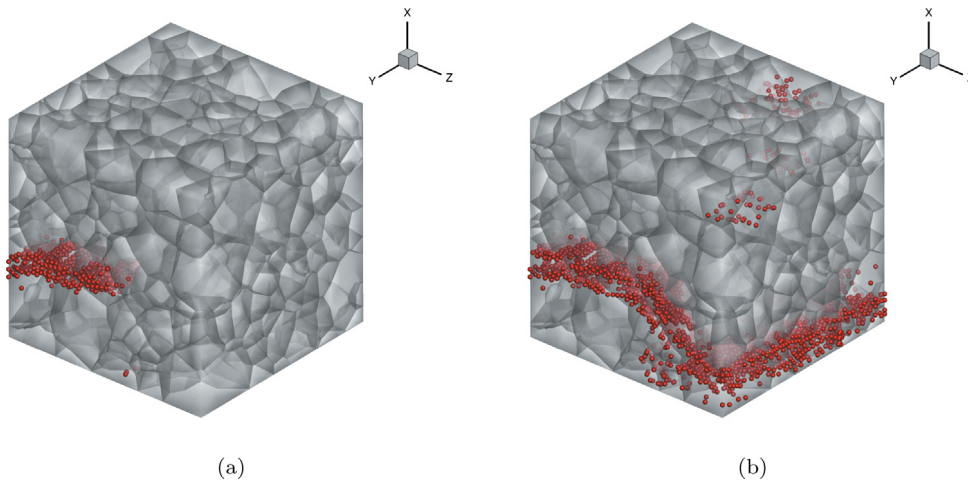


Fig. 17. Location of added nodes associated with second generation wavelet enrichment in the adaptive hierarchical FEM (shown in the undeformed configuration) for ductile fracture of the 512 grain microstructural SERVE at: (a) 5.7% volume-averaged true and (b) 6.4% volume-averaged true strain.

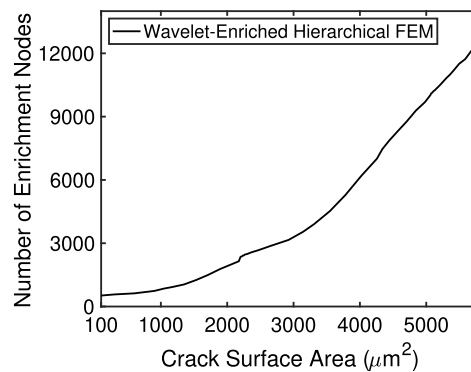


Fig. 18. Evolution of the number of enrichment nodes as a function of the evolving crack surface area.

7. Conclusions

A novel, wavelet-enriched adaptive finite element model is developed in this paper for solving coupled crystal plasticity-phase field models to simulate the crack propagation in polycrystalline microstructures. No *a-priori* assumption of the crack path is needed with this formulation. Crack propagation is driven by stored elastic energy and defect energy resulting from slip system dislocation glide and hardening. The elastic energy terms account for material anisotropy under conditions of finite deformation, as well as tension–compression asymmetry. The defect energy formulation is derived from crystal plasticity models through the principle of maximum plastic dissipation. The elastic and defect energies driving the crack are coupled in the crystal plasticity-phase field variational statements through the use of the principle of virtual power and laws of thermodynamics. The resulting finite element model is capable of simulating both brittle and ductile crack propagation in material microstructures.

A major contribution of this work is the creation of the adaptive, multi-resolution wavelet-based hierarchical enrichment of the FE model, following the path of crack growth. Modeling the evolution of the phase field order parameter s at the length scale of the regularized sharp crack poses a major challenge to the numerical implementation of the coupled crystal plasticity phase field model. For numerical convergence, the coupled model requires the element size in the crack region to be finer than the physical length-scale of the regularized crack, which is significantly smaller than the resolution required for crystal plasticity modeling of grain structures. This requirement is met adaptively in this formulation through the implementation of the lifted second generation wavelet-enrichment in a hierarchical finite element formulation. This formulation projects the solution fields onto a set of scaling and multi-resolution wavelet basis functions. It engages a family of second generation wavelets with a lifting scheme to generate hierarchical interpolation functions that augment the solution by estimating residuals at higher length-scales. By compressing the wavelets to within a prescribed tolerance, it introduces a discretization space, which conforms to the profile of the solution sought, with a desired level of accuracy. This provides an optimal set of hierarchical FE functions that can adaptively enrich the solution space for the crack phase propagation. An iterative solution algorithm, based on static condensation method, is implemented to efficiently calculate an estimate of the solution for the next increment. The estimate is projected to a wavelet interpolation basis, which is then used to form a new solution space.

The wavelet-enriched adaptive finite element model is found to be robust with excellent convergence characteristics in multiple validation tests conducted with the polycrystalline Ti–6V–4Al alloy. Computational studies are conducted with a 42 grain microstructure to comprehend the numerical convergence-rate and computational efficiency. The performance of the wavelet-enriched adaptive FE model is compared with that of a h-adapted adaptive hierarchical FE model. Both brittle and ductile crack propagation are compared with crystal elasticity and crystal plasticity models respectively. For the error estimates, reference solutions are created by using a FE model with an extremely refined uniform mesh. For both cases, the wavelet-enriched adaptive FE model requires significantly less enrichment nodes, and shows a far superior convergence-rate and efficiency. The brittle crack shows a straight crack propagation path with less influence from grain orientations. Ductile crack propagation however shows a high level of dependence of the crack path on the grain slip system orientation. Next the adaptive FE model is tested on a polycrystalline SERVE (statistically equivalent RVE) with 512 grains of the Ti–6V–4Al alloy. The simulations captures the crack propagation behavior in a robust manner with very reasonable computational cost. In summary, this paper has introduced a powerful computational tool for modeling three dimensional crack propagation in polycrystalline microstructures that are governed by finite deformation crystal plasticity relations.

Acknowledgments

This work has been supported by a grant (Grant No. FA-RT1645) by the Division of Naval Materials, Office of Naval Research with Program Directors Dr. William Mullins and Dr. Julie Christodoulou. The authors gratefully acknowledge this support. Computing support by the Homewood High Performance Compute Cluster (HHPCC) and Maryland Advanced Research Computing Center (MARCC) is gratefully acknowledged.

References

- [1] R.A. Lebensohn, N-site modeling of a 3D viscoplastic polycrystal using fast fourier transform, *Acta Mater.* 49 (14) (2001) 2723–2737.
- [2] S.R. Kalidindi, Modeling anisotropic strain hardening and deformation textures in low stacking fault energy fcc metals, *Int. J. Plast.* 17 (6–8) (2001) 837–860.

- [3] F. Roters, P. Eisenlohr, T. Bieler, D. Raabe, *Crystal Plasticity Finite Element Methods in Materials Science and Engineering*, Wiley-VCH, Weinheim, 2010. 1
- [4] A. Shahba, S. Ghosh, Crystal plasticity FE modeling of Ti alloys for a range of strain-rates. Part I: A unified constitutive model and flow rule, *Int. J. Plast.* 87 (2016) 48–68. 2
- [5] P.R. Dawson, M.P. Miller, T.S. Han, J.V. Bernier, An accelerated methodology for the evaluation of critical properties in polyphase alloys, *Met. Trans. A* 36A (2005) 1627–1641. 3
- [6] T. Black, T. Belytschko, A finite element method for crack growth without remeshing, *Internat. J. Numer. Methods Engrg.* 45 (1999) 601–620. 4
- [7] N. Moes, J. Dolbow, T. Belytschko, A finite element method for crack growth without remeshing, *Internat. J. Numer. Methods Engrg.* 46 (1999) 131–150. 5
- [8] I. Babuška, U. Banerjee, J.E. Osborn, Generalized finite element methods: main ideas, results, and perspective, *Int. J. Comput. Methods* 1 (2004) 67–103. 6
- [9] T.P. Fries, T. Belytschko, The extended/generalized finite element method: an overview of the method and its applications, *Int. J. Numer. Methods Eng.* 84 (2010) 253–304. 7
- [10] J. Rungamornrat, M.E. Mear, SGBEM–FEM coupling for analysis of cracks in 3D anisotropic media, *Int. J. Numer. Methods Eng.* 86 (2) (2011) 224–248. 8
- [11] O.C. Zienkiewicz, R.L. Taylor, S.J. Sherwin, J. Peiro, On discontinuous Galerkin methods, *Int. J. Numer. Methods Eng.* 58 (8) (2003) 1119–1148. 9
- [12] R. Abedi, M.A. Hawker, R.B. Haber, K. Matous, An adaptive spacetime discontinuous Galerkin method for cohesive models of elastodynamic fracture, *Int. J. Numer. Methods Eng.* 81 (10) (2010) 1207–1241. 10
- [13] A. Needleman, An analysis of tensile decohesion along an interface, *J. Mech. Phys. Solids* 38 (1990) 289–324. 11
- [14] M. Ortiz, A. Pandolfi, Finite-deformation irreversible cohesive elements for three-dimensional crack-propagation analysis, *Internat. J. Numer. Methods Engrg.* 44 (9) (1999) 1267–1282. 12
- [15] K.L. Roe, T. Sigmund, An irreversible cohesive zone model for interface fatigue crack simulation, *Eng. Fract. Mech.* 70 (2003) 209–232. 13
- [16] K. Park, G.H. Paulino, J.R. Roesler, A unified potential-based cohesive model for mixed-mode fracture, *J. Mech. Phys. Solids* 57 (6) (2009) 891–908. 14
- [17] M. Grujicic, G. Cao, S. Batchu, Crystal plasticity-based finite element analysis of deformation and fracture of polycrystalline lamellar γ -TiAl + α 2-Ti3Al alloys, *J. Mater. Sci.* 38 (2003) 307–322. 15
- [18] H. Tang, Y.S. Choi, A. Acharya, S. Saigal, Effects of lattice incompatibility induced hardening on the fracture behavior of ductile single crystals, *J. Mech. Phys. Solids* 52 (12) (2004) 2841–2867. 16
- [19] S.A. Silling, Reformulation of elasticity theory for discontinuities and long-range forces, *J. Mech. Phys. Solids* 48 (2000) 175–209. 17
- [20] S.A. Silling, O. Weckner, E. Askari, F. Bobaru, Crack nucleation in a peridynamic solid, *Int. J. Fract.* 162 (1–2) (2010) 219–227. 18
- [21] S. Sun, V. Sundararaghavan, A peridynamic implementation of crystal plasticity, *Int. J. Solids Struct.* 5 (19–20) (2014) 3350–3360. 19
- [22] C. Miehe, F. Welschinger, M. Hofacker, Thermodynamically consistent phase-field models of fracture: variational principles and multi-field FE implementations, *Int. J. Numer. Methods Eng.* 83 (2010) 1273–1311. 20
- [23] M. Ambati, T. Gerasimov, L.D. Lorenzis, A review on phase-field models of brittle fracture and a new fast hybrid formulation, *Comput. Mech.* 55 (2015) 383–405. 21
- [24] J.D. Clayton, J. Knap, Phase field modeling of directional fracture in anisotropic polycrystals, *Comput. Mater. Sci.* 98 (2015) 158–169. 22
- [25] Y. Lubomirsky, C. Chen, A. Karma, E. Bouchbinder, Universality and stability phase diagram of two-dimensional brittle fracture, *Phys. Rev. Lett.* 121 (2018) 134301. 23
- [26] Miguel Arriaga, Haim Waisman, Multidimensional stability analysis of the phase-field method for fracture with a general degradation function and energy split, *Comput. Mech.* 61 (1) (2018) 181–205. 24
- [27] Rilin Shen, Haim Waisman, Licheng Guo, Fracture of viscoelastic solids modeled with a modified phase field method, *Comput. Methods Appl. Mech. Engrg.* 346 (2019) 862–890. 25
- [28] B. Bourdin, G.A. Francfort, J.-J. Marigo, Numerical experiments in revisited brittle fracture, *J. Mech. Phys. Solids* 48 (2000) 797–826. 26
- [29] A. Karma, D.A. Kessler, H. Levine, Phase-field model of mode III dynamic fracture, *Phys. Rev. Lett.* 87 (2001) 045501. 27
- [30] J. Bleyer, C. Roux-Langlois, J.F. Molinari, Dynamic crack propagation with a variational phase-field model: limiting speed, crack branching and velocity-toughening mechanisms, *Int. J. Fract.* 204 (1) (2017) 79–100. 28
- [31] M. Hofacker, C. Miehe, A phase field model of dynamic fracture: robust field updates for the analysis of complex crack patterns, *Int. J. Numer. Methods Eng.* 93 (3) (2013) 276–301. 29
- [32] M.J. Borden, C.V. Verhoosel, M.A. Scott, T.J.R. Hughes, C.M. Landis, A phase-field description of dynamic brittle fracture, *Comput. Methods Appl. Mech. Engrg.* 217–220 (2012) 77–95. 30
- [33] M.J. Borden, C.V. Verhoosel, M.A. Scott, T.J.R. Hughes, C.M. Landis, A higher-order phase-field model for brittle fracture: formulation and analysis within the isogeometric analysis framework, *Comput. Methods Appl. Mech. Engrg.* 273 (2012) 100–118. 31
- [34] S. Zhou, T. Rabczuk, X. Zhuang, Phase field modeling of quasi-static and dynamic crack propagation: COMSOL implementation and case studies, *Adv. Eng. Softw.* 122 (2018) 31–49. 32
- [35] T.T. Nguyen, J. Réthoré, J. Yvonnet, M.-C. Baietto, Multi-phase-field modeling of anisotropic crack propagation for polycrystalline materials, *Comput. Mech.* 60 (2) (2017) 289–314. 33
- [36] K. Oshima, T. Takaki, M. Muramatsu, Development of multi-phase-field crack model for crack propagation in polycrystal, *Int. J. Comput. Mater. Sci. Eng.* 03 (02) (2014) 1450009. 34
- [37] Z. Liu, D. Juhre, Phase-field modelling of crack propagation in anisotropic polycrystalline materials, *Proc. Struct. Integ.* 13 (2018) 787–792. 35

- [38] M. Klinsmann, D. Rosato, M. Kamlah, R.M. McMeeking, An assessment of the phase field formulation for crack growth, *Comput. Methods Appl. Mech. Engrg.* 294 (2015) 313–330.
- [39] K.H. Pham, K. Ravi-Chandar, C.M. Landis, Experimental validation of a phase-field model for fracture, *Int. J. Fract.* 205 (2017) 83–101.
- [40] M. Paggi, J. Reinoso, Revisiting the problem of a crack impinging on an interface: a modeling framework for the interaction between the phase field approach for brittle fracture and the interface cohesive zone model, *Comput. Methods Appl. Mech. Engrg.* 321 (2017) 145–172.
- [41] J. Cheng, S. Ghosh, A crystal plasticity FE model for deformation with twin nucleation in magnesium alloys, *Int. J. Plast.* 67 (2015) 148–170.
- [42] J. Cheng, S. Ghosh, Crystal plasticity finite element modeling of discrete twin evolution in polycrystalline magnesium, *J. Mech. Phys. Solids* 9 (2017) 512–538.
- [43] S. Keshavarz, S. Ghosh, Hierarchical crystal plasticity FE model for nickel-based superalloys: sub-grain microstructures to polycrystalline aggregates, *Int. J. Solids Struct.* 55 (2015) 17–31.
- [44] M. Anahid, M.K. Samal, S. Ghosh, Dwell fatigue crack nucleation model based on crystal plasticity finite elements simulations of polycrystalline titanium alloys, *J. Mech. Phys. Solids* 59 (2011) 2157–2176.
- [45] D. Ozturk, A. Shahba, S. Ghosh, Crystal plasticity FE study of the effect of thermo-mechanical loading on fatigue crack nucleation in Titanium alloys, *Fatigue Fract. Eng. Mater. Struct.* 39 (2016) 752–769.
- [46] D. Ozturk, A.L. Pilchak, S. Ghosh, Experimentally validated dwell and cyclic fatigue crack nucleation model for Titanium alloys, *Scr. Mater.* 127 (2017) 15–18.
- [47] H. Chen, C. Zhang, Q. Lu, H. Chen, Z. Yang, Y. Wen, S. Hu, L. Chen, A two-set order parameters phase-field modeling of crack deflection/penetration in a heterogeneous microstructure, *Comput. Methods Appl. Mech. Engrg.* 347 (2019) 1085–1104.
- [48] M. Paggi, M. Corrado, J. Reinoso, Fracture of solar-grade anisotropic polycrystalline silicon: a combined phase field–cohesive zone model approach, *Comput. Methods Appl. Mech. Engrg.* 330 (2018) 123–148.
- [49] C.A.H. Padilla, B. Markert, A coupled ductile fracture phase-field model for crystal plasticity, *Contin. Mech. Thermodyn.* 29 (4) (2015) 1017–1026.
- [50] L. De Lorenzis, A. McBride, B.D. Reddy, Phase-field modelling of fracture in single crystal plasticity, *GAMM-Mitt.* 39 (2016) 7–34.
- [51] A. Shahba, S. Ghosh, Coupled phase field finite element model for crack propagation in elastic polycrystalline microstructures, *Int. J. Fract.* 219 (1) (2019) 31–64.
- [52] X. Shi, H. Huang, G. Cao, X. Ma, Accelerating large-scale phase-field simulations with GPU, *AIP Adv.* 7 (10) (2017) 105216.
- [53] W. Sun, R. Yan, Y. Zhang, H. Dong, T. Jing, GPU-accelerated three-dimensional large-scale simulation of dendrite growth for Ti6Al4V alloy based on multi-component phase-field model, *Comput. Mater. Sci.* 160 (2019) 149–158.
- [54] T. Gerasimov, N. Noii, O. Allix, L. De Lorenzis, A non-intrusive global/local approach applied to phase-field modeling of brittle fracture, *Adv. Model. Simul. Eng. Sci.* 5 (1) (2018) 14.
- [55] L. Demkowicz, Ph. Devloo, J.T. Oden, On an h-type mesh refinement strategy based on a minimization of interpolation error, *Comput. Methods Appl. Mech. Engrg.* 3 (1985) 67–89.
- [56] J.Z. Zhu, O.C. Zienkiewicz, Adaptive techniques in the finite element method, *Commun. Appl. Numer. Methods* 4 (1988) 197–204.
- [57] B.A. Szabo, P.K. Basu, M.P. Rossow, Adaptive finite element analysis based on the p-convergence, *Research in computerized structural analysis and synthesis*, in: *NASA Conf. Publication*, vol. 2059, 1978, pp. 43–50.
- [58] I. Babuska, M. Suri, The p- and h-p version of the finite element method, an overview, *Comput. Methods Appl. Mech. Engrg.* 80 (1–3) (1990) 5–26.
- [59] O.C. Zienkiewicz, J.Z. Zhu, N.G. Gong, Effective and practical h-p version adaptive analysis procedures for the finite element methods, *Int. J. Numer. Methods Eng.* 28 (1–3) (1989) 879–891.
- [60] B. Guo, I. Babuska, The h-p version of the finite element method. Part 1. The basic approximation results, *Comput. Mech.* 1 (1986) 21–41.
- [61] Y. Azdoud, S. Ghosh, Adaptive wavelet-enriched hierarchical finite element model for polycrystalline microstructures, *Comput. Methods Appl. Mech. Engrg.* 321 (2017) 337–360.
- [62] Y. Azdoud, J. Cheng, S. Ghosh, Wavelet-enriched adaptive crystal plasticity finite element model for polycrystalline microstructures, *Comput. Methods Appl. Mech. Engrg.* 327 (2017) 36–57.
- [63] W. Sweldens, The lifting scheme: a construction of second generation wavelets, *SIAM J. Math. Anal.* 29 (2) (1998) 511–546.
- [64] O.V. Vasilyev, S. Paolucci, M. Sen, A multilevel wavelet collocation method for solving partial differential equations in a finite domain, *J. Comput. Phys.* 120 (1) (1995) 33–47.
- [65] O.V. Vasilyev, C. Bowman, Second-generation wavelet collocation method for the solution of partial differential equations, *J. Comput. Phys.* 165 (2) (2000) 660–693.
- [66] A. Staroselsky, L. Anand, A constitutive model for hcp materials deforming by slip and twinning: application to magnesium alloy AZ31B, *Int. J. Plast.* 19 (2003) 843–1864.
- [67] V. Hasija, S. Ghosh, M.J. Mills, D. Joseph, Modeling deformation and creep in Ti-6Al alloys with experimental validation, *Acta Mater.* 51 (2003) 4533–4549.
- [68] D. Deka, D. Joseph, S. Ghosh, M. Mills, Crystal plasticity modeling of deformation and creep in polycrystalline Ti-6242, *Metal. Mater. Trans.* 37 (2006) 1371–1388.
- [69] J.D. Clayton, *Nonlinear Mechanics of Crystals*, Springer, Netherlands, 2011.
- [70] J.-L. Chaboche, Development of continuum damage mechanics for elastic solids sustaining anisotropic and unilateral damage, *Int. J. Damage Mech.* 2 (4) (1993) 311–329.

- [71] H. Amor, J.J. Marigo, C. Maurini, Regularized formulation of the variational brittle fracture with unilateral contact: numerical experiments, *J. Mech. Phys. Solids* 57 (2009) 1209–1229. 1
- [72] M.E. Gurtin, E. Fried, L. Anand, *The Mechanics and Thermodynamics of Continua*, Cambridge University Press, New York, 2010. 2
- [73] Y.F. Gao, A.F. Bower, A simple technique for avoiding convergence problems in finite element simulations of crack nucleation and growth on cohesive interfaces, *Model. Simul. Mater. Sci. Eng.* 12 (3) (2004) 453. 3
- [74] ABAQUS, Dassault systemes ABAQUS/standard user's manual, version 6.9, 2009. 4
- [75] P. Farrell, C. Maurini, Linear and nonlinear solvers for variational phase-field models of brittle fracture, *Int. J. Numer. Methods Eng.* 109 (5) (2017) 648–667. 5
- [76] J. Cheng, A. Shahba, S. Ghosh, Stabilized tetrahedral elements for crystal plasticity finite element analysis overcoming volumetric locking, *Comput. Mech.* 57 (5) (2016) 733–753. 6
- [77] C. Miehe, M. Hofacker, F. Welschinger, A phase field model for rate-independent crack propagation: robust algorithmic implementation based on operator splits, *Comput. Methods Appl. Mech. Eng.* 199 (2010) 2765–2778. 7
- [78] O.C. Zienkiewicz, J.P. De, S.R. Gago, D.W. Kelly, The hierarchical concept in finite element analysis, *Comput. Struct.* 16 (1) (1983) 53–65. 8
- [79] G. Venkatramani, S. Ghosh, M. Mills, A size-dependent crystal plasticity finite-element model for creep and load shedding in polycrystalline titanium alloys, *Acta Mater.* 55 (2007) 3971–3986. 9
- [80] Materials and Processes Engineering Pratt & Whitney, EBSD and tensile & fatigue test data, Private communication, unpublished. 10
- [81] S. Ghosh, A. Shahba and X. Tu, E.L. Huskins, B. Schuster, Crystal plasticity FE modeling of Ti alloys for a range of strain-rates. Part II: Image-based model with experimental validation, *Int. J. Plast.* 87 (2016) 69–85. 11
- [82] M.A. Groeber, M.A. Jackson, Dream.3d: a digital representation environment for the analysis of microstructure in 3d, *Integ. Mater. Manuf. Innov.* 3 (1) (2014) 5. 12
- [83] A. Bagri, G. Weber, J.C. Stinville, W. Lenthe, T. Pollock, C. Woodward, S. Ghosh, Microstructure and property-based statistically equivalent representative volume elements for polycrystalline Ni-based superalloys containing annealing twins, *Metall. Mater. Trans. A* (2018) 1–18. 13
- [84] M. Pinz, G. Weber, W.C. Lenthe, M.D. Uchic, T.M. Pollock, S. Ghosh, Microstructure and property based statistically equivalent RVEs for intragranular $\gamma - \gamma'$ microstructures of Ni-based superalloys, *Acta Mater.* 157 (2018) 245–258. 14